The impact of wind on flow and sediment transport over intertidal flats

Colosimo, Irene; de Vet, Paul L.M.; van Maren, Dirk S.; Reniers, Ad J.H.M.; Winterwerp, Johan C.; van Prooijen, Bram C.

DOI
10.3390/jmse8110910

Publication date
2020

Document Version
Final published version

Published in
Journal of Marine Science and Engineering

Citation (APA)
Colosimo, I., de Vet, P. L. M., van Maren, D. S., Reniers, A. J. H. M., Winterwerp, J. C., & van Prooijen, B. C. (2020). The impact of wind on flow and sediment transport over intertidal flats. *Journal of Marine Science and Engineering*, *8*(11), 1-26. Article 910. https://doi.org/10.3390/jmse8110910

Journal of
Marine Science
and Engineering

MDPI

Article

The Impact of Wind on Flow and Sediment Transport over Intertidal Flats

Irene Colosimo [1,*], Paul L. M. de Vet [1,2], Dirk S. van Maren [1,2], Ad J. H. M. Reniers [1], Johan C. Winterwerp [1] and Bram C. van Prooijen [1]

1 Civil Engineering and Geoscience, Delft University of Technology, Stevinweg 1,
2624 CN Delft, The Netherlands; p.l.m.devet@tudelft.nl (P.L.M.d.V.); Bas.vanMaren@deltares.nl (D.S.v.M.);
a.j.h.m.reniers@tudelft.nl (A.J.H.M.R.); j.c.winterwerp@tudelft.nl (J.C.W.);
B.C.vanProoijen@tudelft.nl (B.C.v.P.)
2 Deltares, Boussinesqweg 1, P.O. Box 177, 2600 MH Delft, The Netherlands
* Correspondence: I.Colosimo@tudelft.nl

Received: 2 October 2020; Accepted: 10 November 2020; Published: 12 November 2020

Abstract: Sediment transport over intertidal flats is driven by a combination of waves, tides, and wind-driven flow. In this study we aimed at identifying and quantifying the interactions between these processes. A five week long dataset consisting of flow velocities, waves, water depths, suspended sediment concentrations, and bed level changes was collected at two locations across a tidal flat in the Wadden Sea (The Netherlands). A momentum balance was evaluated, based on field data, for windy and non-windy conditions. The results show that wind speed and direction have large impacts on the net flow, and that even moderate wind can reverse the tidal flow. A simple analytical tide–wind interaction model shows that the wind-induced reversal can be predicted as a function of tidal flow amplitude and wind forcing. Asymmetries in sediment transport are not only related to the tide–wind interaction, but also to the intratidal asymmetries in sediment concentration. These asymmetries are influenced by wind-induced circulation interacting with the large scale topography. An analysis of the shear stresses induced by waves and currents revealed the relative contributions of local processes (resuspension) and large-scale processes (advection) at different tidal flat elevations.

Keywords: tide–wind interaction; wind-driven flow; sediment transport; intertidal flats; suspended sediment fluxes; sediment storage

1. Introduction

Intertidal flats are habitats of vital importance for numerous flora and fauna species. Migrating birds especially depend on these areas for their survival [1,2]. The flats provide a range of ecosystem services, such as coastal protection, control of erosion, and habitat/fishery linkages [3]. Fragmentation and loss of such environments, and the resulting habitat degradation, are often consequences of human interference [4]. Depending on its future rate, sea level rise may cause the drowning of intertidal areas [5–7]. Management strategies have to be developed to maintain and/or restore intertidal flats, e.g., [8]. Recent studies, e.g., [9–11], show that dredged material can be re-used to feed tidal flats and promote salt marshes restoration. The disposal in estuarine channels can have long-term effects (order of years or decades) on the tidal flats and salt marshes morphodynamics [12]. A detailed understanding of the hydrodynamic and sediment transport mechanisms in intertidal areas is key to predicting their morphological evolution.

Morphological changes are a consequence of spatial gradients in sediment fluxes [13,14] and result from a number of interacting sediment transport processes. These processes depend on hydrodynamic forcing, sediment composition and properties, and biogenic influences [15]. The hydrodynamic forcing is a combination of a deterministic tidal (astronomical) component and a stochastic (meteorological) component. The former induces the daily variation and spring-neap variations in water level and flow velocity. The latter includes the wind forcing. The action of wind on the sea surface results in water level gradients (set-up/down) inducing large-scale circulation patterns (especially in enclosed or semi-enclosed systems such as coastal lagoons or estuaries). Wind blowing on the sea surface also generates wind-waves, which induce turbulence resulting in sediment resuspension from the seabed. Wind waves interact with the (tide- and wind-induced) currents, modifying the bed roughness and ultimately affecting the bed shear stress induced by the flow [16,17]. Furthermore, wind-driven flows are related to wind induced shear stress penetrating the water column.

While the combined effect of wind events and tides has received significant attention in the scientific literature, e.g., see [18–24], these studies focused primarily on the relative impacts of wave-induced erosion and tide-induced accretion. However, the role of wind-driven flows, and especially the interaction between tidal currents and wind-driven flow, has received much less scientific attention. It has been demonstrated that wind-driven flows affect the tide-induced velocities and suspended sediment concentrations on the Belgian inner shelf (thereby influencing the position of the turbidity maximum [25]). Observations by Christiansen et al. [26], Mariotti and Fagherazzi [27], and Talke and Stacey [28] demonstrate that different meteorological conditions generate asymmetries in the intratidal sediment transport. In multi-inlet lagoons such as the Wadden Sea, the wind-induced fluxes result in water and sediment exchange over the tidal divides, leading to an inter-connected morphodynamic evolution of the adjacent tidal basins [29,30]. However, even though these studies demonstrate the importance of wind-driven flows, it remains unclear how wind-driven flows interact with tidal currents, and how this interaction subsequently impacts residual sediment transport.

In the present study we used field data obtained on a meso-tidal mudflat in the Western Wadden Sea and we developed an analytical model to explain the tide-wind interaction at different elevations of the tidal flat. More specifically, we aimed to: (i) quantify the interaction between tidal and wind-driven flow at different elevations on the intertidal flat (upper and lower flat); (ii) understand the effect of wind on the suspended sediment concentration (SSC); and (iii) understand the consequences of wind-induced modification of flow and SSC on the suspended sediment fluxes (SSF). The paper is structured as follows. Specifications about the study site, the field data collection, and the methodology used for the suspended sediment flux (SSF) estimation are given in Section 2. The time series of the measured variables are provided in Section 3. In Section 4 an analytical tide–wind interaction model is developed and applied. Further, the effect of tide and wind on residual sediment fluxes is quantified. The effects of this interaction on the SSC and the SSF are discussed. Conclusions are given in Section 5. Appendix A shows the wave–current interaction model used to compute the shear stresses at the bottom.

2. Material and Methods

2.1. Study Area

The area of investigation is a fringing mudflat located in the Vlie tidal basin (Dutch Wadden Sea, The Netherlands). This basin is connected to the North Sea via an inlet between the islands Vlieland (west) and Terschelling (east); see Figure 1. The tidal inlet develops into a fractal-type branching channel system ending in the so-called Kimstergat channel, close to the Harlingen harbor. The Dutch Wadden Sea is a meso-tidal lagoon with a mean tidal range of 2 m, measured at the tidal gauge of Harlingen. Spring-neap tidal variations in water level are significant (S2/M2 = 0.25). Furthermore, the water level can vary significantly due to surges in the North Sea, in addition to water level gradients developing within the multi-inlet lagoon system. The considered mudflat is located near the village Koehool, along the Dutch coast, 15 km northeast of the harbor of Harlingen. The Koehool mudflat lies at the north-east edge of the Kimstergat tidal channel. This tidal channel, oriented parallel to the coast, forms a connection for water and sediment transport between the Harlingen harbor and the mudflat area. The 2 km wide mudflat is mildly sloped, approximately 1:1000. In the last century the relatively sheltered location favored the accumulation of very fine sediment [9]. Its median diameter ranges from 100 μm at the lower mudflat (close to the channel) to 30 μm at the higher mudflat zone (close to the shore). A similar decrease in median grain size and an increase in mud content from the deeper foreshore towards the higher mudflat has been observed in other studies, e.g., [15,31,32]. The Kimstergat tidal channel influences the hydrodynamics and sediment transport on the Koehool mudflat. Fresh water discharge some ∼15 km south of the harbor affects the transport in the deeper zones of the channel, resulting in seaward-directed baroclinic sediment transport [33]. The contribution of this baroclinic circulation significantly weakens in the shallower areas of the channel (depth < 3 m) [33], and can be therefore neglected on the (even shallower) intertidal areas.

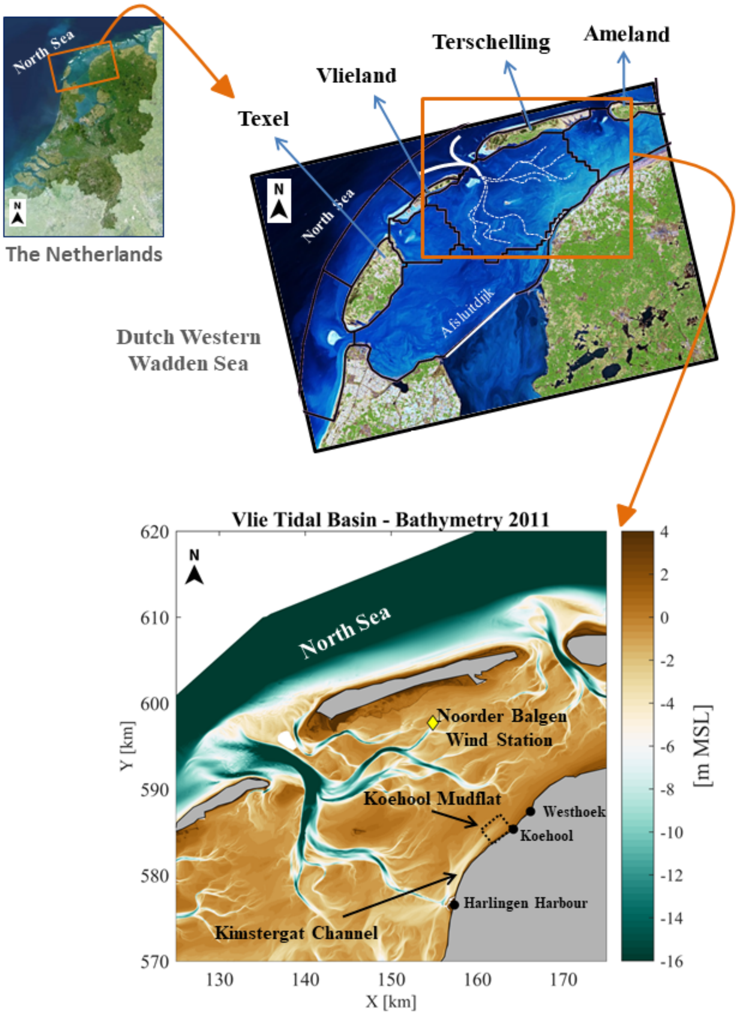

Figure 1. Study area. Top figures: The Western Wadden Sea is located in the northern part of the Dutch coast. Four barrier islands and the Afsluitdijk are indicated (satellite image: Deimos Imaging SLU, an UrtheCast company). The boundaries of the tidal basins (i.e., the tidal divides) are indicated in black. Bottom figure: the Vlie tidal basin bathymetry in 2011. The bathymetric data are part of the Vaklodingen dataset (available on www.OpenEarth.nl). Latitude and longitude are expressed in the Rijks Driehoeken (RD) system; the bed elevation is indicated with respect to mean sea level (MSL). White color in the top left corner indicates absence of data. Mainland and islands are in gray. The Noorder Balgen meteorological station, used as the source of wind data, lies at ∼5 km offshore the study site.

2.2. Field Measurements

Two measuring frames were installed along a cross-shore transect on the Koehool mudflat (Figure 2) from 14 April till 23 May 2016. One frame was located at the lower flat (indicated hereafter as F_{LM}, abbreviation of "frame lower mudflat"). The other frame was located at the higher mudflat zone (indicated hereafter as F_{HM}, or "frame higher mudflat"). F_{LM} was placed at ~1 km from the land boundary, at a bed elevation of 0.97 m below MSL (mean sea level), i.e., close to mean low water (MLW), which means an almost 100% submergence time. F_{HM} was installed at 350 m from the land boundary, at a bed elevation of −0.27 m MSL, with a submergence time of ~60%.

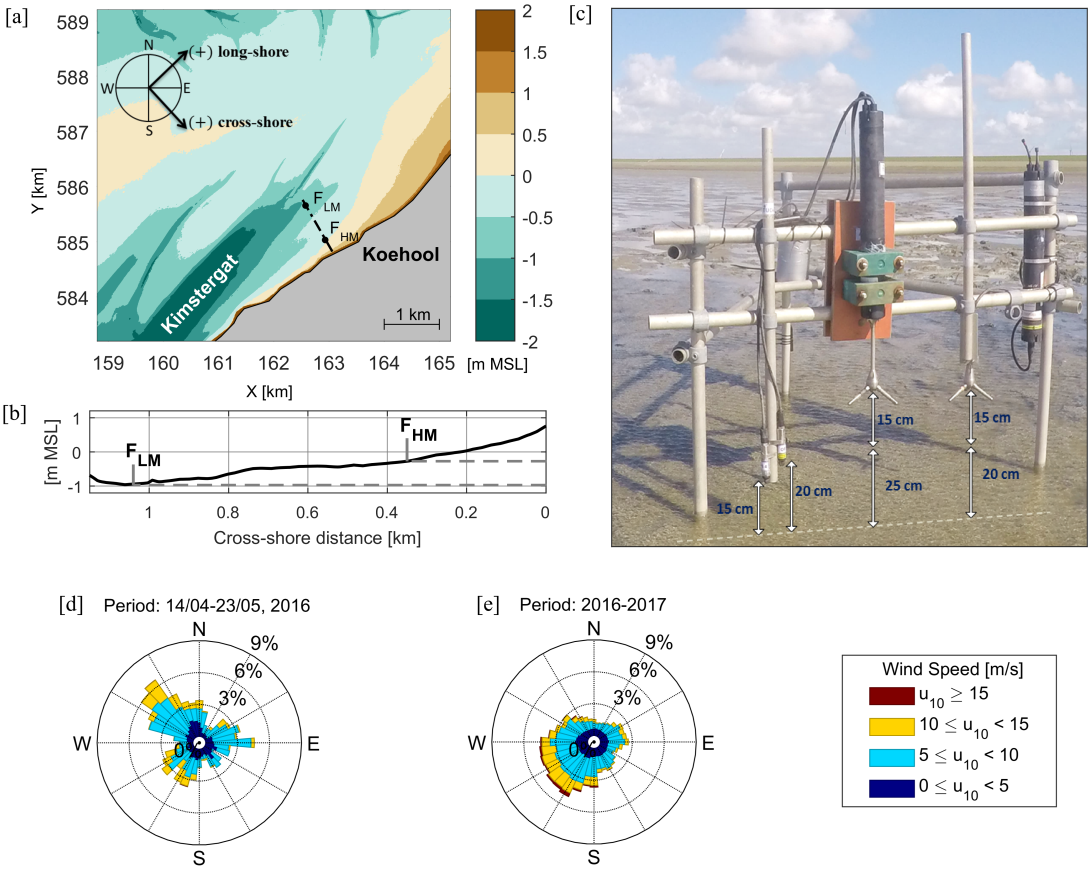

Figure 2. Study sites and wind forcing. (**a**) Measuring sites at the Koehool mudflat transect: lower mudflat frame (F_{LM}) and higher mudflat frame (F_{HM}). The bed levels are from the 2011 bathymetry. The sign convention for long-shore and cross-shore flow is provided in the top left corner. (**b**) Transect cross-shore profile with the elevations and distances from the land boundary of the two frames. (**c**) Picture of the higher mudflat frame (F_{HM}) with indication of the distances of sensors from the bed, including the 15 cm blanking distances of the ADVs (i.e., the distance of the measurement volume from the instrument probe). (**d**,**e**) Wind roses referring, respectively, to the deployment period and to the period January 2016–December 2017.

At each frame, two ADVs (acoustic doppler velocimeters, Nortek Vector) were installed to perform point-measurements at 20 cm and 25 cm above the bed. Both ADVs measured at a frequency of 8 Hz. The ADVs at 20 cm from the bed were used to measure the flow velocity in continuous mode, whereas the ADVs at 25 cm from the bed were set to measure in burst mode. These ADVs were configured to measure with 20-min burst intervals, with 4800 samples/burst at F_{LM}, and 2400 samples/burst at F_{HM}. This means that the ADV at F_{LM} measured during 10 min out of the 20-min long burst interval and the ADV at F_{HM} during 5 min out of the same interval. The ADV measures the distance of the probe from the bed (i.e., the bed elevation) at the beginning and end of each burst, thereby providing bed level measurements every 20 min at both sites.

Two OBSs (Optical Back Scatter, Campbell3+) were mounted at each station at 15 and 20 cm above bed (see Figure 2). The OBSs at 15 cm from the bed were meant as duplicates for validation purposes, which explains the short vertical distance between the two sensors. The backup OBSs showed almost identical values to the OBSs installed at 20 cm above the bed; the latter were used in the data analysis.

In close proximity to each frame, one pressure sensor (OSSI-010-003C, Ocean Sensor Systems) was installed at 5 cm above the bed, with the aim of providing further wave measurements (used to check and validate the ADV pressure measurements). These sensors were configured to measure in continuous mode with a frequency of 10 Hz.

The frames were installed for a total of 39 days. At each frame one extra-battery package (AWAC) with 920 kWh energy capacity was connected to the ADVs measuring in a continuous mode. At F_{LM} the battery was sufficient to measure for 36.5 days. At F_{HM} the battery dropped after 28 days. The data were therefore processed for 73 tidal cycles at F_{LM} and 56 tidal cycles at F_{HM}. Every two weeks the frames were inspected and no bio-fouling was detected on the sensors. At each inspection the bed elevation at the two sites and the sensors' distances from the bed were measured using a differential GPS (DGPS-Leica GS14).

Wind data at 10-min intervals were obtained from the meteorological station Noorder Balgen, situated in the Western Wadden Sea tidal basin (see Figure 1). This station is located 15 km offshore from the measurement sites and no land boundaries separate the meteorological station from the two sites. Air pressure variation information was not available at the Noorder Balgen station, so that the air pressure data gathered at the Leeuwarden meteorological station (situated 20 km in-land from the study site) were used.

The 10-min frequency water levels data measured at the tidal gauge of Harlingen harbor (15 km south the investigated sites) were also used in the analysis.

2.3. Data Post-Processing

The flow velocity signals were de-spiked following the methodology proposed by Goring and Nikora [34]. The sensors were not always submerged during the full tidal cycle. The emerged periods were filtered out using the amplitude and beams correlation given by the ADV signals. Thresholds for the amplitude signal of 100 counts and a beam correlation of 70% were applied.

The pressure signals from ADVs and OSSI sensors were corrected for the variations in air-pressure. The pressure data provide information on water levels and waves. The astronomical components of the water levels were estimated applying the harmonic analysis proposed by Codiga [35] (U-Tide matlab function) on the Harlingen tidal gauge signal.

The ADV pressure signals, combined with the flow velocity information, were used to carry out a directional wave spectral analysis. The OSSI pressure sensors were used to provide a non-directional wave spectral analysis. Although the first analysis provides more detailed information, it is only available for a reduced portion of the tidal cycle. In fact, the ADV pressure sensors were placed at large distances from the seabed (up to 55 cm), due to the constraint of measuring the velocity at 20 cm from the seabed. In contrast, the OSSI pressure sensors provide less information, but given the reduced distance of the sensors from the bed (i.e., 5 cm), this information is available for almost the full period that the bed was submerged. Therefore, the wave heights and wave periods resulting from the directional analysis were used only for validation of the results obtained from the non-directional analysis. The wave parameters obtained from the non-directional wave spectral analysis, more specifically the significant wave height and the mean period of the 33% highest waves following [36], were used.

The OBSs were calibrated in the laboratory, using sediment-laden water samples collected in the field (maximum SSC 15 g/L, i.e., higher than maximum SSC measured in the campaign). These samples were collected in proximity to the higher mudflat frame, while holding a sample at $\sim$30 cm from the bed and simultaneously inducing sediment resuspension by eroding the upper seabed layers. The procedure in the laboratory included synchronized OBS measurements in a 8 L calibration bowl and sample filtration through 0.45 µm pore filters. Thirty dilution steps were carried out. At each step a sample of 500 mL of the sediment-laden water was extracted from the calibration bowl and replaced by 600 mL of clear water. Through this process, the initial sediment-laden water was reduced to almost clear-water. After each dilution step the OBS data (voltage) were collected for a 5-min period, and during this period, a 100 mL sample was taken in proximity to the optical sensors. These samples were filtered and the filters were dried for 24 h in an oven at 105 °C. The filters were weighted before and after the filtration procedure, so that given the volume of the sample (100 mL) the sediment concentration (in g/L) was established. The pattern in the calibration curves shows a linear relationship up to 1 g/L ($R^2 \approx 0.97$), whereas a quadratic regression can better describe the relationship for SSC above this threshold ($R^2 \approx 0.95$).

2.4. Suspended Sediment Flux Estimate

The depth-integrated suspended sediment flux (SSF) is defined by integrating the product of the velocity profile and the sediment concentration profile over the water column. We expect a logarithmic profile for flow velocity and a Rouse profile for the SSC distribution over the vertical. Continuous measurements are, however, only available at 20 cm above the bed. We therefore approximate the SSF by assuming that the velocity and SSC measured at 20 cm above the bed are representative of the depth-averaged values:

$$SSF(t) = h(t) \cdot u_{20}(t) \cdot SSC_{20}(t) \tag{1}$$

with long-shore or cross-shore flow velocity u_{20} and suspended sediment concentration SSC_{20} at 20 cm above the bed and h water depth. The effects of the vertical distribution of the velocity and sediment concentration on the fluxes were therefore not taken into account. A similar approach was followed in Andersen and Pejrup [37]. The suspended sediment flux has been integrated to estimate the fluxes cumulated over a tidal-cycle:

$$\int_0^{T^*} SSF(t) = \int_0^{T^*} h(t) \cdot u_{20}(t) \cdot SSC_{20}(t) \tag{2}$$

where the time scale T^* is based on the submergence time per tide (hence not necessarily equal to the tidal period). The minimum water level was used to separate two subsequent tides in case the bed did not emerge. These integrated fluxes can be interpreted as the net flux per tide.

2.5. Definitions and Conventions

We define the long-shore and cross-shore directions based on the topographic (contour) lines at the two locations (Figure 2). At both sites the contour is oriented along the SW–NE axis direction (with deviations smaller than 10%). Hence, we consider the flow in the SW–NE direction as long-shore flow, and the flow in the SE–NW direction as cross-shore flow. The local coordinate system is shown in Figure 2a. In the long-shore direction, the flow is up-channel during flood and down-channel during ebb. In the cross-shore direction, the flow is onshore-directed during flood and offshore-directed during ebb.

In this paper we consider a "flow reversal" a situation in which the wind induces a flow direction opposite to the tide-only direction of the flow. We therefore define a "reversed flood" as a period with rising water and with down-channel long-shore flow and offshore-directed cross-shore flow. Vice versa, we define a "reversed ebb" as a falling-water period with up-channel long-shore flow and onshore-directed cross-shore flow.

The standard nautical definition is used for the wind direction, e.g., SW wind indicates wind blowing from the SW towards the NE direction.

3. Results

3.1. Full-Period Time Series

The time series of wind speed and direction, water depth, long-shore and cross-shore flow velocity, significant wave height, and SSC are shown in Figure 3 for the lower mudflat (F_{LM}) and in Figure 4 for the higher mudflat (F_{HM}).

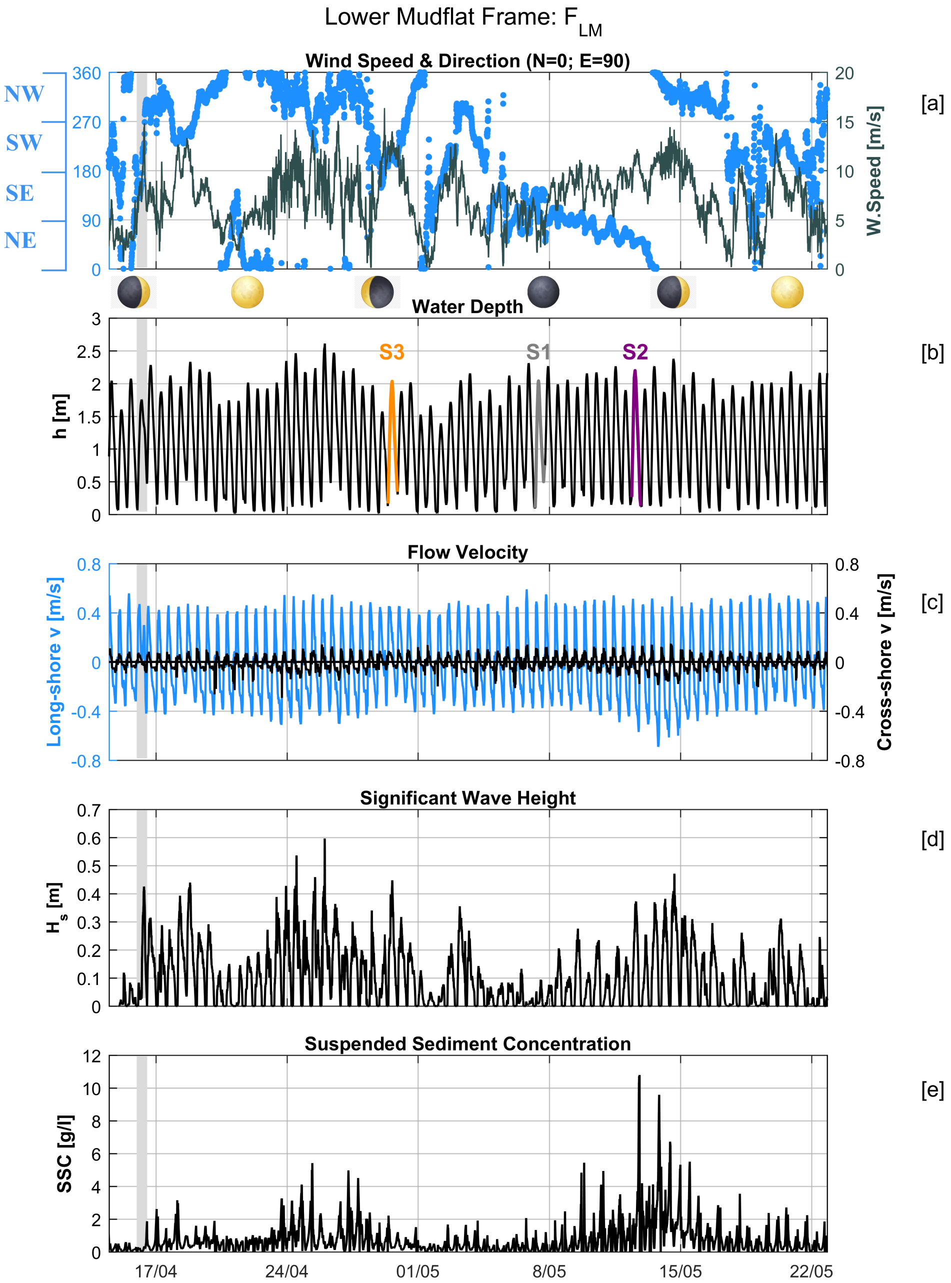

Figure 3. Time series at the lower mudflat (F_{LM}): (**a**) Wind speed and direction; (**b**) Water depth (moving mean over 10-min intervals); (**c**) Long-shore and cross-shore flow velocities; (**d**) Significant wave height; (**e**) Suspended sediment concentration. Spring-neap variations are indicated by the moon phases. The gray bands indicate the tides affected by the wind-induced reversal of ebb flow. The tides indicated by S1, S2, and S3 are used in Section 3.2 to analyze the intratidal variations during three different wind scenarios.

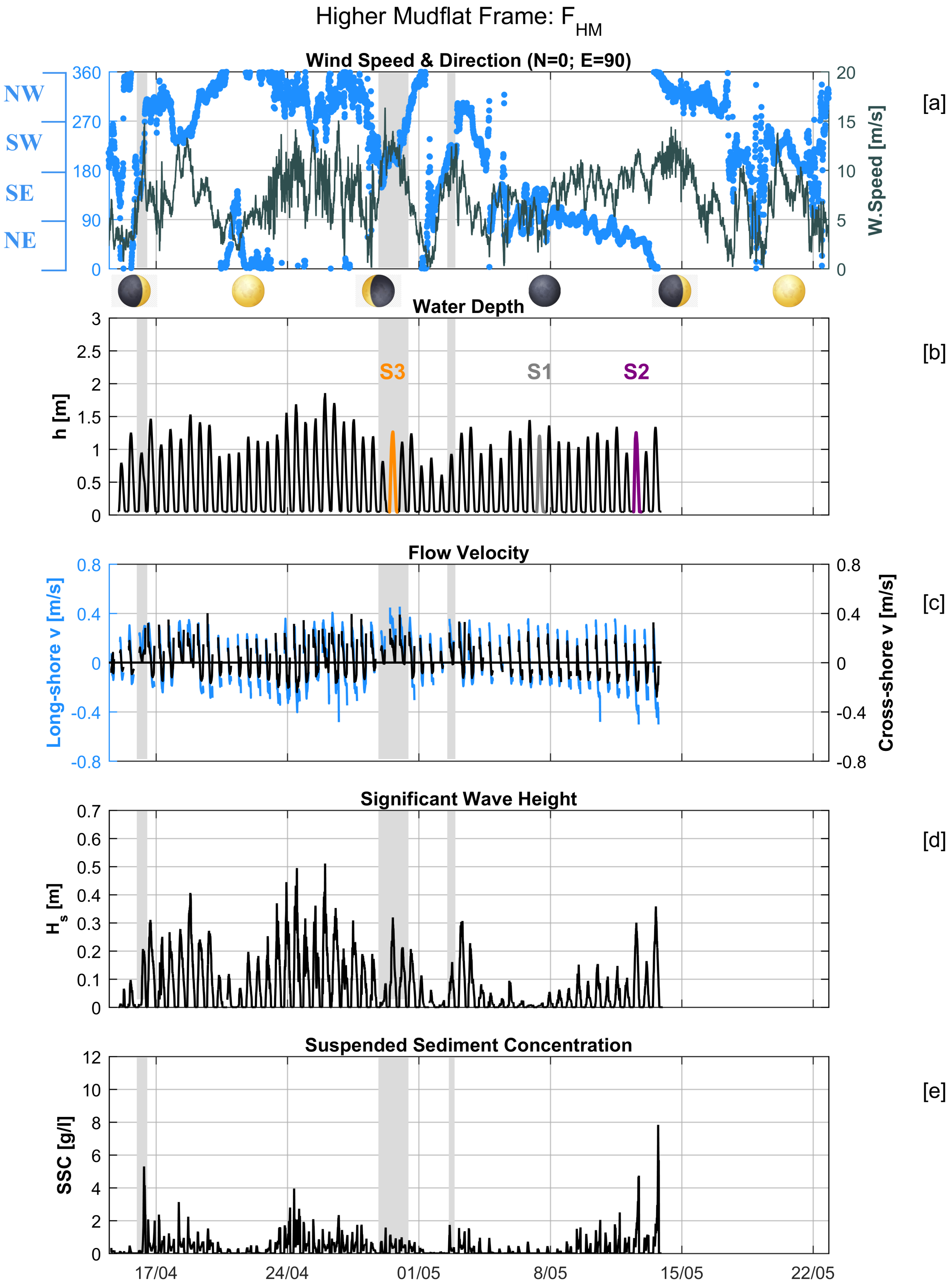

Figure 4. Timeseries at the higher mudflat (F$_{HM}$): (**a**) Wind speed and direction; (**b**) Water depth (moving mean over 10-min intervals); (**c**) Long-shore and cross-shore flow velocities; (**d**) Significant wave height; (**e**) Suspended sediment concentration. Spring-neap variations are indicated by the moon phases. The gray bands indicate the tides affected by the wind-induced reversal of ebb flow. The tides indicated by S1, S2, and S3 are used in Section 3.2 to analyze the intratidal variations during three different wind scenarios.

The average wind speed (Figure 3a or Figure 4a) was 7 m/s, and the mean of the 5% highest values was 14 m/s. The maximum wind speed was 16 m/s and it occurred in SW wind direction. The dominant wind direction during the measurement period was NW, and the maximum wind speeds (16.4 m/s) had SW wind direction. Based on the wind roses in Figure 2d,e it is noticed that along a year instead, the dominant wind direction is SW.

The water depth (Figures 3b and 4b) depends on the tide and on a wind-induced water level set-up. Increased water levels occur for example in the period 24–28 April for NW wind of ∼13 m/s.

The tidal flow amplitude (Figures 3c and 4c) is ∼0.5 m/s at F_{LM} and ∼0.25 m/s at F_{HM}. The flow at F_{LM} is mainly directed in the long-shore direction (NE–SW). The cross-shore component magnitude (SE–NW) is ∼20% of the long-shore flow. At F_{HM}, the cross-shore component is much larger (both relatively and absolutely), with a magnitude comparable to the long-shore flow velocity component. In Figure 4c the large variations in flow velocity are evident: the flow is not necessarily flood-directed (positive) and then ebb-directed (negative) during each tidal cycle. During several periods of falling water (i.e., during ebb), the flow remains up-channel (i.e., flood-directed). These reversed ebb flow conditions are caused by wind-driven flow and occur during wind from the SW (i.e., wind parallel and opposite to the ebb flow). The reversal conditions are highlighted in Figures 3a,c and 4a,c by gray colored bands. In particular, Figure 4c shows that the tidal flow was up-channel during three consecutive tidal cycles (29–30 April). This wind-induced reversal of the ebb flow occurred during 17% of the monitored period at the higher mudflat (F_{HM}) but only once (1.3% of the time) at the lower mudflat (on 16 April).

Maximum wave heights were observed during maximum water levels (Figures 3d and 4d), resulting from a larger fetch (related to the submergence of the shoals) and weaker bed friction at larger depths. The highest significant wave height was 0.6 m on both sites. The wave conditions are dominated by the local wind, because the barrier islands shelter the study area from North Sea (swell) waves.

The SSC varies throughout the tidal cycle (Figures 3e and 4e), with values ranging from several g/L during low water conditions (i.e., at the end of the ebb phase) to values in the order of 10^{-2}–10^{-3} g/L during maximum water depth. The highest SSC values did not coincide with the largest wave height, but coincided instead with high wind speeds blowing during low water conditions (up to 8 and 12 g/L at the F_{HM} and F_{LM}, respectively).

3.2. Three Selected Wind Scenarios: Analysis of Wind-Induced Tidal Flow Reversal

In order to isolate the effects of wind on the tide-induced flow, SSC, and SSF, we selected three representative wind scenarios: one scenario with weak wind (S1, $u_{10} < 5$ m/s) and two scenarios with long-shore directed wind, i.e., NE wind (S2, ebb directed) and SW wind (S3, flood-directed). The latter two scenarios exhibit the wind-effects on the flow when the tidal and wind forcings are aligned. These three scenarios occurred on May 7 (S1), May 12 (S2), and April 29 (S3), respectively, as indicated in Figures 3 and 4 and detailed at intratidal time scale in Figures 5 and 6.

Scenario S1 is characterized by the formation of a standing wave, with maximum flow velocities during maximum gradients in water level (generally occurring when the water level is around MSL). Flood velocities are generally higher than ebb velocities and the falling water phase lasts longer (8 h) than the rising water phase (4 h). This implies a peak flow asymmetry in flood direction. This Eulerian asymmetry in peak flow velocities is modified when the wind enhances tidal flow velocities, as discussed in detail hereafter.

In scenario S1, the weak offshore directed wind resulted in significant wave heights smaller than 0.1 m (Figures 5b and 6b). The tide-averaged wind speed during scenario S3 was slightly higher (12 m/s) compared to S2 (10.6 m/s). In scenario S3 this high wind speed persisted for 12 consecutive hours, whereas in scenario S2 the wind speed was above 10.6 m/s during the 67% of the tidal cycle. As a consequence, the significant wave height peaks were ∼10 cm higher during scenario S3 than S2.

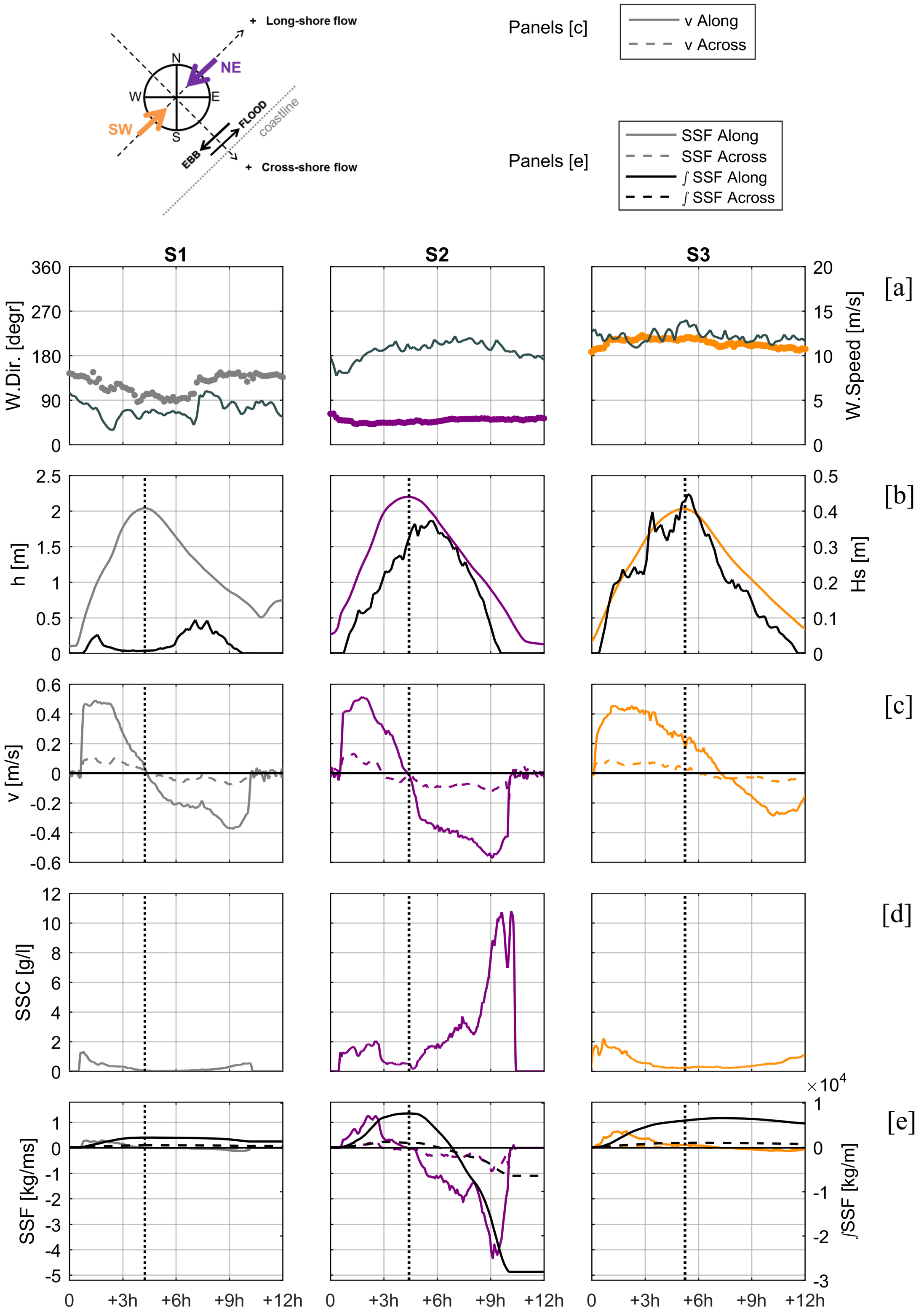

Figure 5. Intra-tidal variation at the lower mudflat (F_{LM}) in three wind scenarios: S1 (weak wind); S2 (ebb-directed wind); S3 (flood-directed wind). (**a**) Wind speed (solid line) and direction (markers); (**b**) Water depth and significant wave height (black solid line); (**c**) Flow velocity in the long-shore direction and cross-shore direction; (**d**) Suspended sediment concentration (SSC); (**e**) Left axis: suspended sediment flux (SSF) in long-shore and cross-shore directions; right axis: time-integrated suspended sediment flux ($\int$ SSF) in long-shore and cross-shore directions.

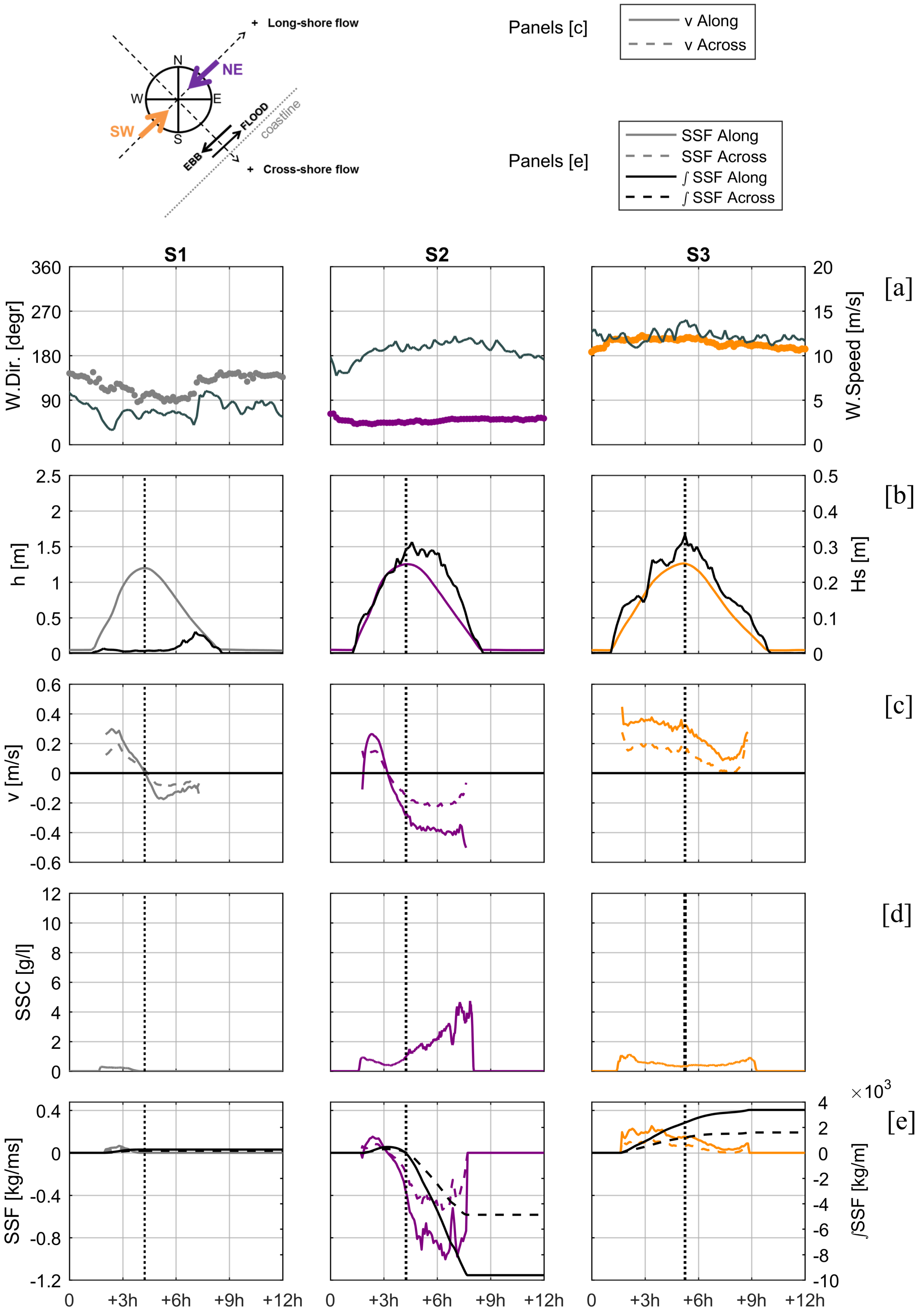

Figure 6. Intra-tidal variation at the higher mudflat (F_{HM}) in three wind scenarios: S1 (weak wind); S2 (ebb-directed wind); S3 (flood-directed wind). (**a**) Wind speed (solid line) and direction (markers); (**b**) Water depth and significant wave height (black solid line); (**c**) Flow velocity in the long-shore direction (solid line) and cross-shore direction (dashed line); (**d**) Suspended sediment concentration (SSC); [**e**] Left axis: suspended sediment flux (SSF) in long-shore and cross-shore directions; right axis: time-integrated suspended sediment flux ($\int$ SSF) in the long-shore and cross-shore directions.

During scenario S2, wind from the NE enhances the ebb flow, increasing the peak long-shore flow velocity by more than 20 cm/s at both sites, thereby becoming ebb-dominant. During scenario S3 the flow generated by the opposing wind reverses the tidal flow: during part of the ebb phase at F_{LM} and during the full cycle at F_{HM}. The vertical dotted lines in Figures 5 and 6 indicate the moment of high water, which at F_{LM} in scenarios S1 and S2 corresponds to slack water conditions. In scenario S3 at F_{LM} the wind opposing ebb delays slack water and consequentially increases the length of flood directed flow by about three hours. At F_{HM} in scenario S2 the flood phase is shortened by about one hour due to the opposite NE wind, whereas in scenario S3 the flood-directed flow persisted during the full tidal cycle.

The Eulerian asymmetries in the hydrodynamic forcing affect the intratidal asymmetries in SSC (Figures 5d and 6d). During no-wind conditions (S1) the flow is flood dominant and SSC values are larger during flood than during ebb. Ebb flows at F_{HM} were not strong enough to transport or resuspend sediment, and therefore the SSC was zero. The intratidal variation of SSC was especially asymmetric during scenario S2. The maximum in SSC during ebb increased by up to 10 g/L and 4 g/L at F_{LM} and F_{HM}, with respect to the S1 scenario. Interestingly, despite larger wave heights and comparable water levels, the maximum SSC during scenario S3 was much smaller than during S2.

The effect of wind on the SSF variation is comparable for the two locations. As the water depth, flow velocity, and SSC are larger at F_{LM}, the resulting SSF are one order of magnitude larger at F_{LM} than at F_{HM} (note the different vertical axes in the two figures). The magnitude of the cross-shore sediment transport (dashed lines) is smaller than the long-shore transport (solid lines), but the response to wind action of the two components is similar. The SSF was considerably higher during scenario S2. The time-integrated SSF at the end of the tidal period (representative for the residual transport over the tide) increased up to three orders of magnitude compared to scenario S1 at F_{LM}. During scenario S3, at F_{HM} the reversed ebb resulted in a flood-directed residual transport (3.4×10^3 kg/m) one order of magnitude larger compared to scenario S1 (2.5×10^2 kg/m). In scenario S2 the (ebb-directed) net flux (-9.6×10^3 kg/m) increased by almost three orders of magnitude compared to S1.

3.3. Sediment Transport, Bed Shear Stress and Bed Level Change

The wind-induced effects on water depth, flow velocity and SSC resulted in a large variability in SSF (Figure 7b,c). No clear spring-neap variation is observed in the SSF during the deployment period. The time-integrated SSF indicates that over the full period the net transport was negative (sediment export) at F_{LM} and slightly positive (sediment import) at F_{HM}.

Figure 7d,e indicate that the bed shear stress related to currents is larger at F_{LM} than at F_{HM} (submerged period average 0.25 Pa and 0.17 Pa, respectively) whereas the wave-induced shear stresses are higher at F_{HM} than at F_{LM} (submerged period average 0.63 Pa and 0.33 Pa, respectively).

The change in bed elevations (Figure 7f) shows that over the full deployment period the bed eroded 1 cm at F_{LM} while it increased 6 cm in elevation at F_{HM}. Comparing the two sites, the bed level is highly dynamic at the higher mudflat and more stable at the lower mudflat.

At F_{HM} increasing time-integrating fluxes correspond mainly to increases in bed elevation (orange boxes in Figure 7c,f), vice versa decreasing time-integrated fluxes corresponds mainly to decreases in bed elevation (purple boxes in Figure 7c,f). This alignment in trends is absent at F_{LM} (purple and orange boxes in Figure 7b,f). Furthermore, at F_{LM} the magnitude of the instantaneous SSF is larger than at F_{HM}, but the smaller net fluxes (less influenced by wind) result in a less dynamic bed. The data also suggests a minor effect of waves on bed level changes at F_{LM}: SW wind results in relatively high wave-related bed shear stress (up to 4 pa), but not necessarily in bed erosion.

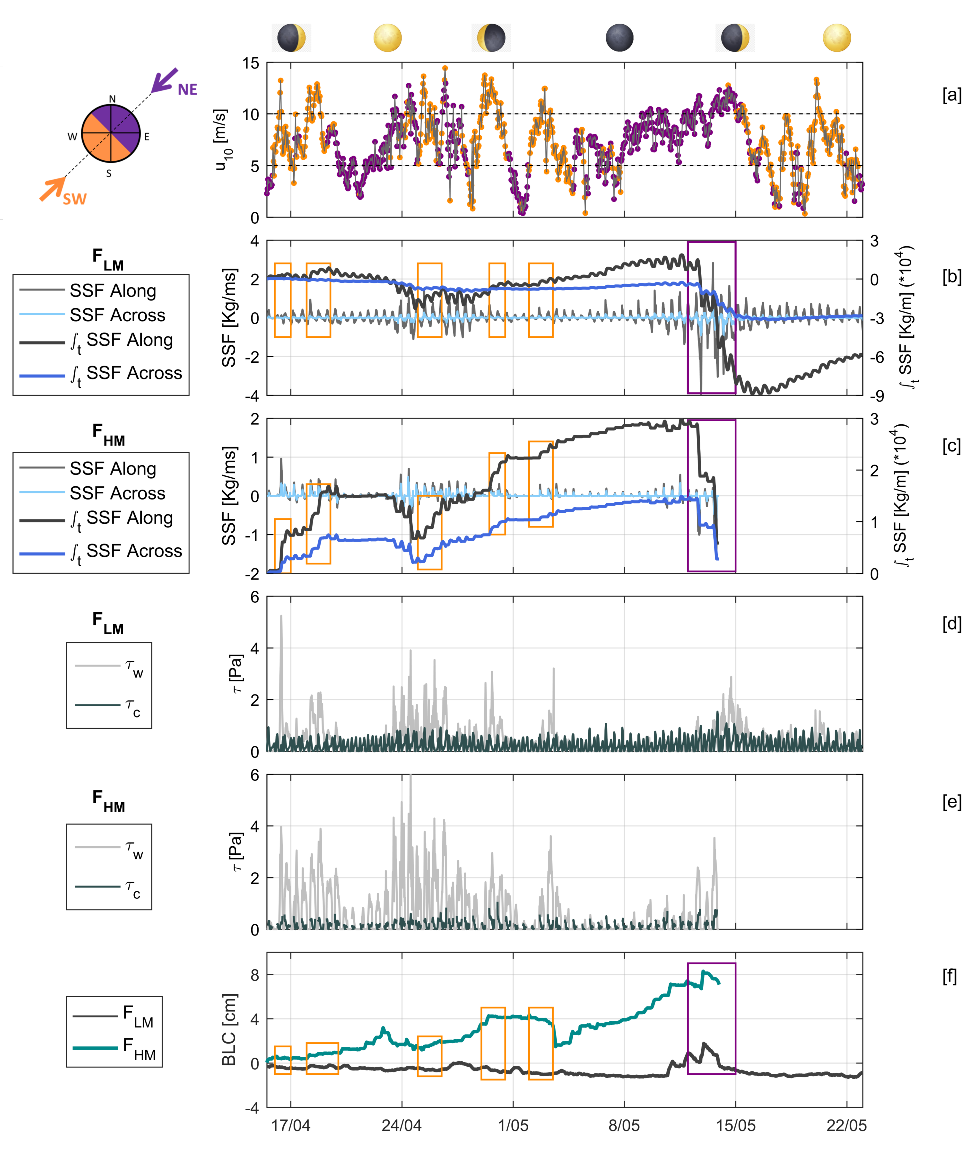

Figure 7. (**a**) Wind speed u_{10} and direction (color of the markers); (**b**,**c**) Long-shore and cross-shore SSF and time-integrated SSF in the positive (up-channel) and negative (down-channel) direction, respectively at F$_{LM}$ and F$_{HM}$; (**d**,**e**) Current and wave induced shear stresses, respectively at F$_{LM}$ and F$_{HM}$; (**f**) Bed level change. The value of the bed elevation is indicated as zero at the beginning of the measurement period. The boxes indicate specific wind events for which the boxes are colored orange in case of SW wind and purple in case of NE wind.

4. Discussion

4.1. Determination of Leading Order Terms in the Momentum Balance Equation

Section 3 revealed the prominent role of wind in modifying the flow velocity at the two study sites, especially on the higher mudflat. In this section, we quantify the mechanisms explaining this difference using the depth-averaged momentum balance equation (MBE) in the dominant flow direction:

$$\rho_w h \frac{\partial u_x}{\partial t} - \rho_a c_D u_{10}|u_{10}| + \rho_w c_{f_{wc}} u_x|u_x| + \rho_w g h \frac{\partial \eta}{\partial x} + \rho_w u_x h \frac{\partial u_x}{\partial x} = 0 \tag{3}$$

with the density of seawater $\rho_w = 1020\ \mathrm{kg/m^3}$; water depth h; long-shore flow velocity u_x; time t; density of air $\rho_a = 1.23\ \mathrm{kg/m^3}$; wind drag coefficient c_D; wind speed at 10 m above the surface u_{10};

bed friction coefficient related to waves and currents $c_{f_{wc}}$; gravitational acceleration g and water level η. The first three terms in Equation (3) can be determined from the time series of the variables measured at the two sites.

The first term in Equation (3) represents inertia and can be estimated using the time series of the water depth and the long-shore flow velocity measured at 20 cm from the seabed.

The second term is the stress induced by the wind on the sea surface, computed using the wind speed time-series. The dimensionless wind drag coefficient typically ranges between 0.001 and 0.002 for wind speed between 5 m/s and 20 m/s, e.g., [38]. This coefficient can be estimated from the wind speed [39,40]:

$$c_D = \frac{\rho_a}{\rho_w} \cdot (a + b \cdot u_{10}) \tag{4}$$

with a and b coefficients as estimated by Wu [40]: $a = 0.8$, $b = 0.065$. The mean value of the drag coefficient obtained for the measurement period is 0.015, which corresponds well to values found in literature. As we compute the momentum balance in the long-shore direction, we evaluate the case of wind in the same direction (positive when blowing in the flood direction).

The third term represents the current-induced bed shear stress. The coefficient c_{f_w} represents the exchange of momentum between the bed and the water, and depends on the combined effect of current and waves. Waves modify the vertical profile of the flow velocity resulting in a net bed shear stress in addition to the current-induced shear stress. The friction coefficient by waves and currents $c_{f_{wc}}$ is defined as (Soulsby [41] and Faria et al. [16]):

$$c_{f_{wc}} = \frac{\tau_m}{\rho_w u^2} \tag{5}$$

with τ_m is the mean bed shear stress by currents and waves and u the depth-averaged flow velocity. The mean bed shear stress τ_m is estimated using the model proposed by Soulsby [41], as elaborated in detail in Appendix A. Its mean value during the field experiment was 0.0034 at F_{LM} and 0.0025 at F_{HM}, respectively.

The fourth term represents the barotropic pressure gradient, which is composed of two components: a time-averaged component (resulting in water level set-up/-down) and a time-varying component (related to the propagation of the tidal wave). The former cannot be established from the local time-series, so it remains excluded from our balance. The latter can be estimated from the celerity $c = \sqrt{gh}$, so that the spatial water level gradient can be computed from its temporal gradient:

$$\rho_w g h \frac{\partial \eta}{\partial x} \approx -\rho_w \sqrt{gh} \frac{\partial \eta}{\partial t} \tag{6}$$

The fifth term represents advection and requires estimation of the spatial velocity gradient, for which we apply the approach of Equation (6) as well:

$$\rho_w u_x h \frac{\partial u_x}{\partial x} \approx -\rho_w u_x h \frac{1}{\sqrt{gh}} \frac{\partial u_x}{\partial t} \tag{7}$$

Advection in the cross-shore direction has been neglected as the cross-shore gradient of the long-shore velocity $(\partial u_x / \partial y)$ is relatively small. Substituting these estimates into Equation (3) gives:

$$\rho_w h \frac{\partial u_x}{\partial t} - \rho_a c_D u_{10} |u_{10}| + \rho_w c_{f_{wc}} u_x |u_x| - \rho_w \sqrt{gh} \frac{\partial \eta}{\partial t} - \rho_w u_x h \frac{1}{\sqrt{gh}} \frac{\partial u_x}{\partial t} + \mathrm{res} = 0 \tag{8}$$

with 'res' a residual term, representing errors in the estimations and the terms that could not be computed using the time series.

In Figure 8 the five terms are presented for the three wind scenarios. Advection ($O(10^{-3})$) and inertia ($O(10^{-2})$) are small compared to the wind-induced stress, the bed shear stress, and the pressure gradient ($O(10^{-1})$).

Figure 8 suggests that three dominant terms in the MBE are: the wind induced stress, the bed shear stress, and the (time-varying) pressure gradient. Furthermore, comparing the scenarios S2–S3 with scenario S1, Figure 8 shows that an increase in wind-induced stress is mainly compensated by a higher bed shear stress. Differently from the bed shear stress, the pressure gradient does not show a clear variation with wind-shear stress.

Figure 8 also reveals that wind has a more pronounced effect in modifying the tide-induced flow at F_{HM} than at F_{LM}: the velocity at F_{HM} is positive (i.e., flood-directed) during the full tidal cycle for S3, while the same wind conditions did not fully reverse the ebb flow at F_{LM}. The mechanisms responsible for this difference are explored in the next section via the development of a tide-wind interaction model (Section 4.2) which is subsequently compared to the data (Section 4.3).

The different terms do not result in a closure of the balance, leading to a residual. The residuals are also shown in Figure 8. These residuals reflect: (1) the terms that cannot be estimated from a point-measurement; (2) assumptions in the definitions of the bed shear stress term and wind shear stress term, including the uncertainties in the related to the coefficients $c_{f_{wc}}$ and c_D, and (3) measurement inaccuracies. The residuals have similar magnitudes as the dominant terms, implying that the excluded terms (especially the time-varying pressure gradient, given the relatively small advection values in the long-shore direction) play a role in the momentum balance. If we compare the residuals of S1 and S2 for F_{LM}, a similar pattern is found. No clear influence of the wind can be identified. In S3, instead, the residuals partly compensate for the wind induced shear stress. This is, however, not the case for S3 at F_{HM}: at this site, the residuals have the same sign as the wind shear stress. No particular general pattern could be deduced from the time variation of the residual. High resolution numerical modeling could provide more insights into the residual term.

4.2. Tide–Wind Interaction Model

Figure 8 indicates that the time-varying pressure gradient, the bed shear stress, and the wind shear stress are three dominant terms in the momentum balance. In this section we elaborate on the balance of these three terms in windy and non-windy conditions. We especially aim at exploring the interaction between these terms and the implications for the flow velocity.

In absence of wind, a balance is assumed between the time-varying pressure gradient and the bed shear stress; i.e., the flow velocity is purely tide-induced, i.e., $u_x \equiv u_T$:

$$\rho_w g h \frac{\partial \eta}{\partial x} = -\rho_w c_{f_{wc}} u_T |u_T| \tag{9}$$

The wind (S2, S3) induces a considerable shear stress at the surface (up to 0.4 Pa in S3). The balance therefore requires an additional wind-induced shear stress and a bed shear stress generated by tides and wind (i.e., $u_x \equiv u_{TW}$):

$$\rho_w g h \frac{\partial \eta}{\partial x} = \rho_a c_D u_{10} |u_{10}| - \rho_w c_{f_{wc}} u_{TW} |u_{TW}| \tag{10}$$

The pressure gradient term due to the tide – first term in Equation (10) – follows from Equation (9), as this term is hardly influenced by the wind; see Figure 8:

$$-\rho_w c_{f_{wc}} u_T |u_T| = \rho_a c_D u_{10} |u_{10}| - \rho_w c_{f_{wc}} u_{TW} |u_{TW}| \tag{11}$$

Equation (11) is an approximation of the MBE in which u_T and u_{TW} are now explicit. We emphasize that the effect of water level set-up/-down is not included here. This implies that the flow velocity u_{TW} is to be considered as an upper limit.

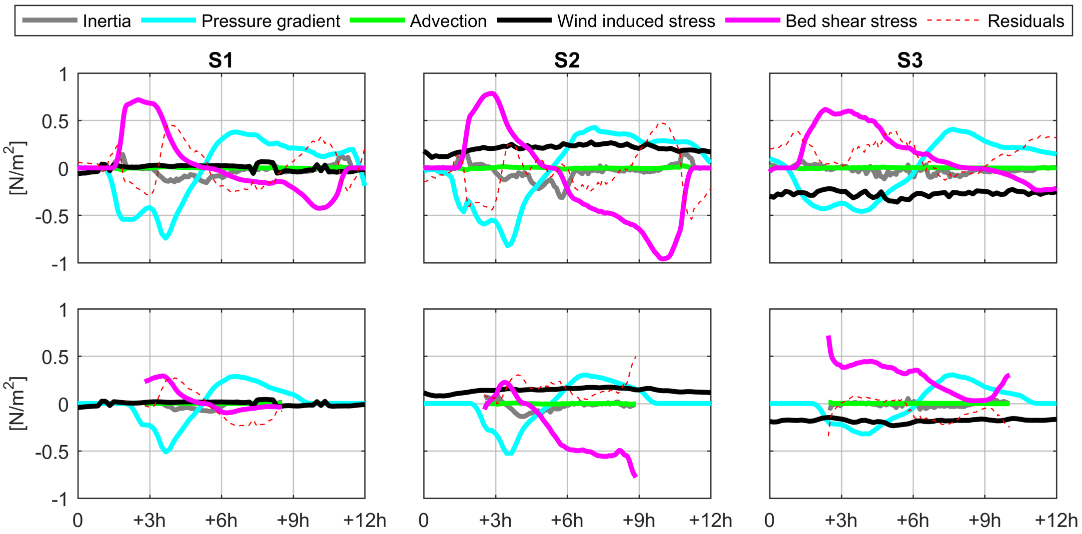

Figure 8. Terms of the momentum balance equation in the three wind scenarios (S1–S3 from left to right) at the lower mudflat (F$_{LM}$, **upper panels**) and higher mudflat (F$_{HM}$, **bottom panels**). The terms include the sign given in Equation (3).

Rearranging Equation (11) yields an expression for the velocity due to tides and wind, expressed as the sum of the two components:

$$u_{TW}|u_{TW}| = \underbrace{u_T|u_T|}_{\text{TIDE}} + \underbrace{\frac{\rho_a c_D}{\rho_w c_{fwc}} u_{10}|u_{10}|}_{\text{WIND}} \tag{12}$$

This relation is explored for a sinusoidal tide $u_T = \hat{u}\sin\left(\frac{2\pi}{T}t\right)$, with velocity amplitude $\hat{u}$ and tidal period T. To keep the model simple, we use the mean time-invariant value of the friction coefficient $c_{fwc} = 0.00285$. The velocity due to tide and wind u_{TW} can thus be computed for a given wind speed (Figure 9).

The two panels of Figure 9 present two contrasting cases of wind in flood direction (Figure 9a) and in ebb direction (Figure 9b). The mean u_{TW} decreases for increasing $\hat{u}$, implying that the effect of wind-driven flow is smaller when the "background" (pressure-induced) tidal flow is larger. Wind in flood direction (Figure 9a) leads to a non-linear summation of tidal and wind-driven flow during flood, and in the opposite direction during ebb. During both flood and ebb, u_{TW} is larger for higher wind speed. However, the wind-driven flow is less effective at larger tidal flow amplitude, so that u_{TW} tends to the value of u_T (black lines with 1:1 slope). In cases of opposing wind, the u_{TW} during ebb can be positive (i.e., reversed in flood direction). These results are confirmed by observations at the two sites, the tidal flow amplitudes of which are indicated by gray dashed lines. Figure 9 suggests flow reversal at F$_{HM}$ at wind velocities exceeding ∼10 m/s, which corresponds to the observations in Figure 6. The figure suggests that a wind speed of ∼20 m/s should reverse the ebb flow at the lower mudflat (F$_{LM}$), but such a wind speed (and flow reversal) did not occur during our field campaign.

Two specific hydrodynamic conditions in the tide-wind interaction model require attention. The first is the absence of tidal flow ($\hat{u} = 0$ m/s). This condition equals the first order estimate derived in De Vet et al. [42]. The second is the zero-flow condition ($u_{TW} = 0$ m/s, indicated by black markers). Zero-flow corresponds to the turning point for wind-induced tidal flow reversal: the tidal flow and wind-driven flow are equal in magnitude. This condition implies that the wind shear stress equals the pressure gradient related to the tide. The two cases are therefore related: for a given wind velocity, u_{TW} at $u_T = 0$ m/s is equal to $\hat{u}$ at $u_{TW} = 0$ m/s. This implies that for constant wind conditions, the flow velocity u_{TW} at zero tidal flow is equal to the wind-driven flow $\hat{u}$ required to reverse the tidal flow. The circular-like shape of the ebb curves when wind blows in flood direction, and for the flood curves when wind blows in ebb direction, results from Equation (12) getting the form of a circumference equation: $x^2 + y^2 = r^2$. For $u_{10} > 0$ the circular-like shape exists for $u_T < 0$, i.e., during ebb; and for $u_{10} < 0$ the circular-like shape exists for $u_T > 0$, i.e., during flood.

The interaction between tidal and wind-driven flow also depends on the tidal asymmetry, which is only marginally important for our case. In case of flood dominance, the wind is more effective in modifying the ebb; and in cases of ebb-dominance the flow velocity during flood will be more sensitive to the wind-induced modifications (at the same wind speed). The tide–wind interaction results in modified asymmetries in peak flow velocity during flood and ebb. Therefore, the effect of the wind on the flow depends on the Eulerian asymmetries in the astronomical signal (being stronger for small tidal asymmetry) and affects the Eulerian asymmetries in the meteorological signal (possibly reversing the flow during flood or ebb).

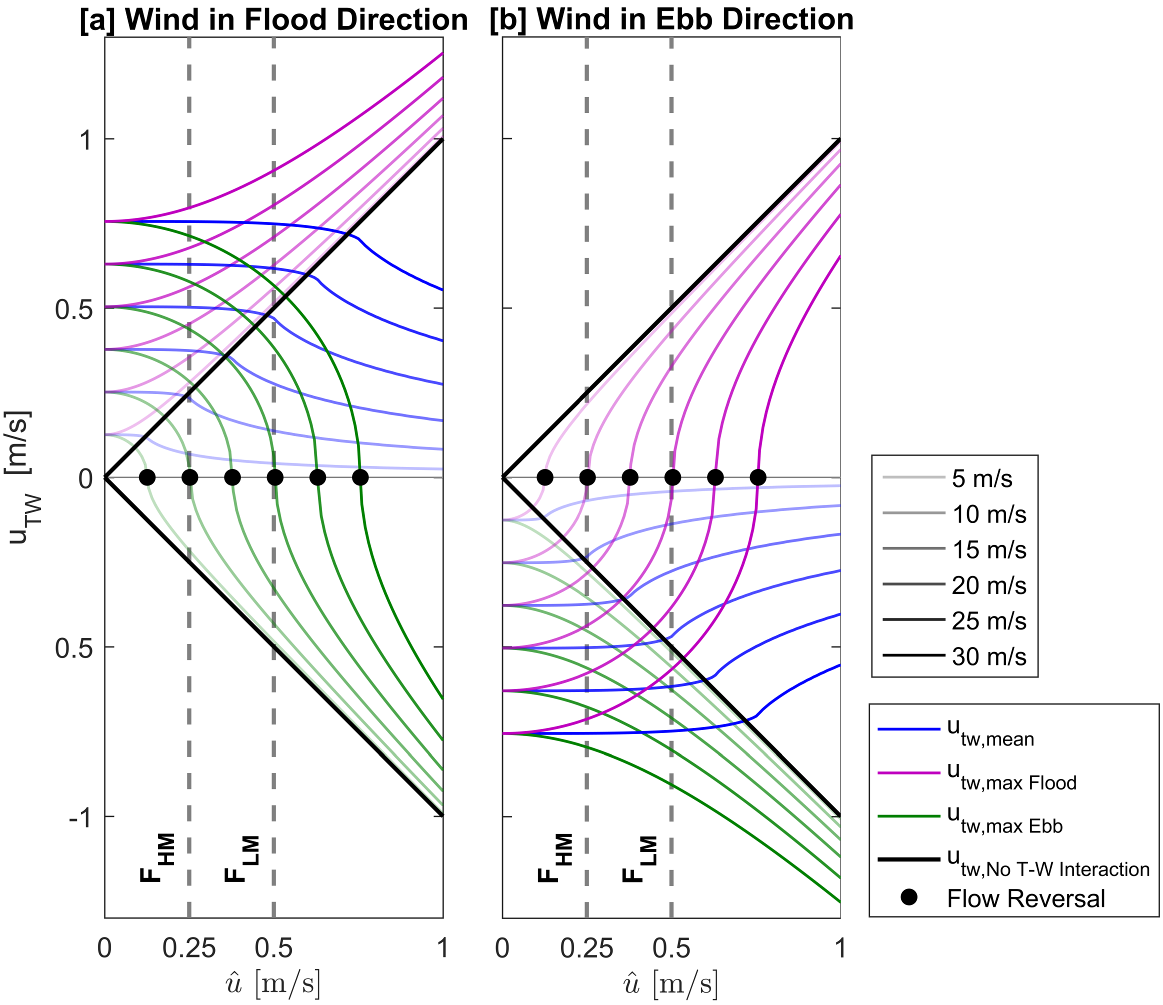

Figure 9. Tide–wind interaction model results. Tide-averaged flow velocity resulting from the interaction of tidal flow and wind-driven flow (u_{TW}) as a function of the tidal flow amplitude ($\hat{u}$). (**a**) Wind is in flood direction; (**b**) Wind is in ebb direction. The tide-averaged velocity (blue) and the maximum tide-averaged velocity during flooding (pink) and during ebb flow (green) are computed as functions of the tidal flow amplitude. The case of no interaction between tide and wind is represented by the dashed lines. The flow tidal amplitudes at the F_{HM} and F_{LM} are 0.25 and 0.5 m/s, respectively. The black markers indicate the turning points for wind-induced reversal of the tidal flow.

4.3. Effect of Wind on Tide-Averaged Flow: Model and Data Comparison

This tide–wind interaction model was verified using data from the full measurement period (Figure 10). For wind speeds close to zero the observed tide-averaged flow velocity is close to zero, whereas tide-averaged flow velocities increase with higher wind speeds. Although the absolute flow velocity is larger at F_{LM} than at F_{HM}, the net flow is strongest at F_{HM}. The direction of the net flow is determined by the wind direction: not only long-shore directed winds, but also wind non-parallel to the flow (e.g., NW or SE) enhance flood and ebb currents in their main direction (i.e., long-shore direction). This effect results from the bathymetry of the channel, forcing the flow to align with the main tidal channel flow.

The dashed lines in Figure 10 indicate the computed tide-averaged velocity by wind over a still body of water, i.e., without tide–wind interaction: $\langle u_{TW} \rangle = \frac{\tau_W}{\rho_w c_{fcw}}$. Including the tide–wind interactions (solid line) the net flow depends on the tidal amplitude also (for which we use typical values of $\hat{u} = 0.5$ m/s at F_{LM} and $\hat{u} = 0.25$ m/s at F_{HM}).

Both the solid and the dashed lines represent conditions where the wind is exactly in stream-wise direction and persists during the full tidal cycle, and are therefore upper limits of the wind effect. At F_{HM} the dashed and the solid lines are closer than at F_{LM}. On the higher mudflat the tidal flow is small (0.25 m/s), and even weak winds are able to influence the net flow. On the lower mudflat, the lines diverge because of the larger tidal flow (0.5 m/s), resulting in stronger non-linear interactions between the two components, and therefore in weaker net flows.

The model shows good agreement with the observations, highlighting the difference in the tide–wind interaction at the different elevations of the mudflat. Contrary to the approximation by De Vet et al. [42], this model predicts the flow velocity, including the interaction between tidal flow and wind-driven flow. The contribution of such a mechanism is key for predicting net flow velocities at larger tidal flow velocities. The relative and absolute influence of the wind on the flow decreases with increasing tidal flow.

In order to asses the model's applicability to other locations and environments, the assumptions made are discussed hereafter. Firstly, the model is based on Equation (12) in which we neglected the contribution by the residuals in the MBE, and especially the component related to the wind-induced pressure gradient. The model does include the barotropic pressure gradient related to the tide. It does not, however, include changes in the pressure gradient by wind, which would induce a time-averaged water level set-up/-down. We expect this contribution to be relevant in semi-enclosed systems like coastal lagoons or in estuaries, where solid land boundaries allow the development of a spatial pressure gradient. In such systems, the wind shear stress is to a larger extent counterbalanced by a pressure gradient. The Wadden Sea tidal basin shape is elongated in the direction of the dominant wind direction (see Figure 1): the land boundaries in the NE and SW result in smaller set-ups with wind blowing in the long-shore direction (e.g., the dominant wind direction, SW) compared to the boundaries in the cross-shore direction.

Secondly, a term excluded from the MBE was the advection of the long-shore velocity in cross-shore direction. Given the magnitude of advection in the main velocity direction, we do not expect that this term plays an important role. However, this term is expected to have more relevance at tidal flats which are more elevated relative to MSL. In this case, refraction of the tidal wave on the coastal shelf would increase cross-shore flows on the higher flat.

Thirdly, a constant (time-averaged) value for the drag coefficient and the bed friction coefficients is used. This assumption was based on an assessment of the time-dependency of the drag and friction coefficients not reported here (see as a reference [43]), which showed consistency with values suggested in the literature.

Even though this assessment suggests that the temporal variability of the drag and friction coefficients was sufficiently small to use values typical for the full observation period, the model might be further improved by including the time-dependence of these parameters.

We conclude that the representation of the momentum balance equation by three terms (pressure gradient term, bed friction, and wind forcing) shows that there is a strong non-linear interaction. The influence of the wind diminishes for increasing tidal flow. Furthermore, the model provides a simple algebraic formulation for the estimation of flow reversal.

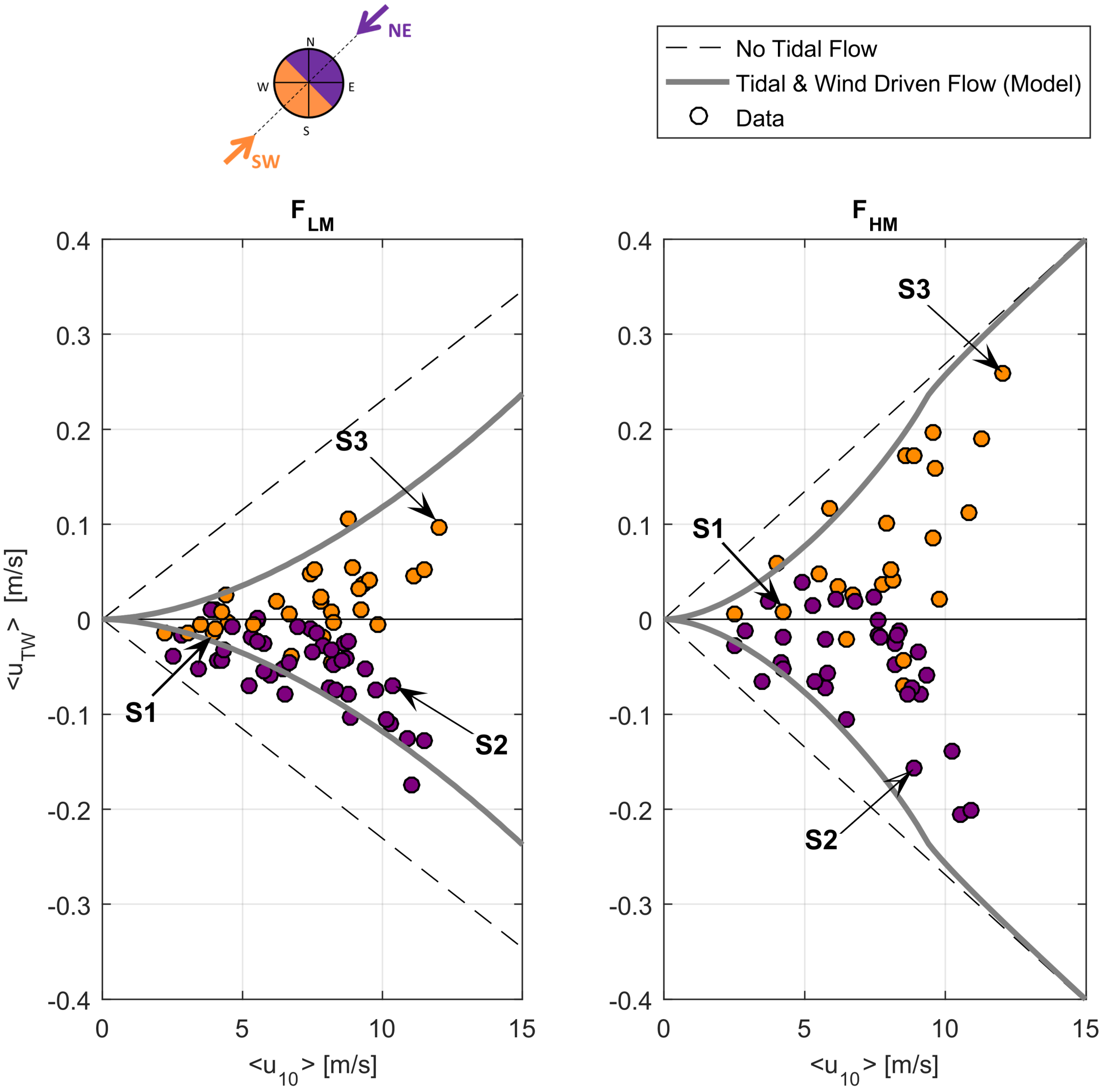

Figure 10. Flow velocity resulting from the interaction of tidal flow and wind driven flow as a function of wind speed. The dashed lines indicate u_{TW} in case of no interaction between tide and wind-driven flow; the solid lines represent u_{TW} accounting for the tide–wind interaction. The tidal flow amplitude was set as 0.5 m/s at F_{LM} and 0.25 m/s at F_{HM}. The drag coefficient was set as $c_D = 0.0015$, i.e., the mean value of the time-dependent drag coefficient during the full measurement period. The bed friction coefficients were set as $c_{f_{cw}} = 0.0034$ at F_{LM} and $c_{f_{cw}} = 0.0025$ at F_{HM}, i.e., the mean value of the time-dependent wave–current bed friction coefficient during the full measurement period. Each marker represents the long-shore flow velocity averaged during one tide. Positive values in the figure imply flood-directed net flow; negative values imply ebb-directed net flow. The color of the marker indicates the dominant wind direction during the tide. The tides representing the three wind scenarios are indicated.

4.4. Resuspension and Advection by Currents and Waves

In order to generalize the impact of wind on SSC to a wider range of wind conditions, we analyze tide-averaged wind direction and speed, bed shear stresses, and SSC in more detail. From Figure 11c–f it was noticed that both at F_{LM} and F_{HM} the SSC increases with wind speed (larger circles at higher wind velocities). For low wind speed (u_{10} < 3 m/s), the tide-averaged SSC is ∼0.8 g/L at F_{LM}, and ∼0.3 g/L at F_{HM}. Hence, during tide-only conditions, the sediment concentration is higher on the lower flat than on the higher flat.

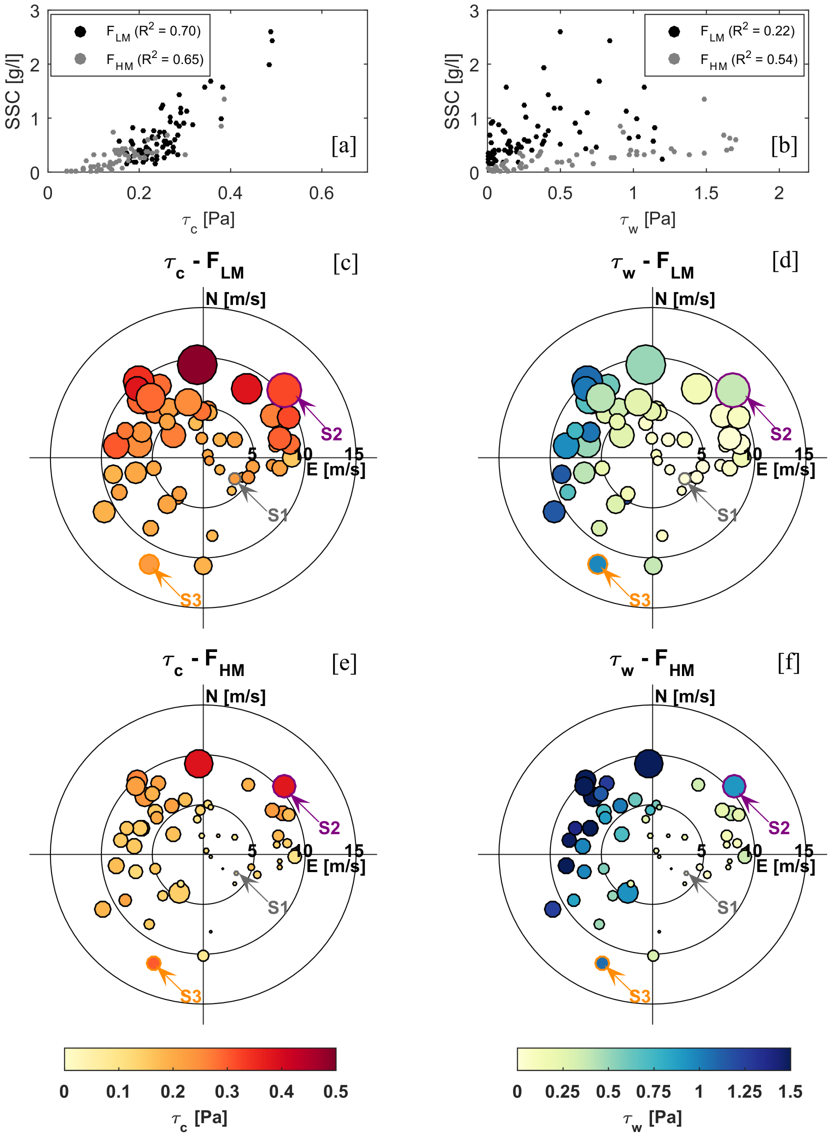

Figure 11. Tide-averaged wind conditions, bed shear stresses, and SSC. (**a**,**b**) Tide averaged SSC versus tide-averaged current shear stress and wave shear stress, respectively. The coefficients of determination R^2 for the linear regressions applied to (**a**,**b**) are indicated in the legends. (**c**,**f**) SSC-bed shear stress-wind roses: each marker corresponds to one tide (i.e., tide-averaged values are used). The positions of the markers in the rose are representative of the wind conditions during the tide: tide-averaged wind speed and dominant wind direction (e.g., marker position in the upper right quadrant implies a dominant wind from NE). The color of the marker indicates the tide-averaged current-induced shear stress (**c**,**e**) or wave-induced shear stress (**d**,**f**). The sizes of the markers scale with the tide-averaged SSC. The tides of the three wind scenarios are indicated. In the panels dedicated to F_{LM}, only the 56 tides measured at F_{HM} are included.

At F_{LM} the SSC increases with the current-induced bed shear stress (i.e., darker markers have a larger size in Figure 11c). Such a trend is present, but less evident, at F_{HM} (Figure 11e). The effect of the wave-induced stress is instead more evident at F_{HM} (i.e., darker markers have a larger size in Figure 11f) compared to F_{LM} (Figure 11b). Apparently, variations in SSC at the higher mudflat are both related to currents and waves, whereas at the lower mudflat variations in SSC are primarily the results of a high current-induced bed shear stress. Figure 11a,b provides statistical information to quantify this difference in the relative contribution of current-induced and wave-induced shear stress to SSC. The current-induced shear stress explains 70% and 65% of the variance in SSC, respectively, at F_{LM} and F_{HM}, highlighting the contribution of sediment advection at both sites. Differently, the analysis indicates that the wave-induced shear stress explains 54% of the SSC variance at F_{HM} and only 22% of the SSC variance at F_{LM}, confirming what was observed in the SSC-wind roses, i.e., that the contribution of the resuspension to the sediment concentration is poor at the lower mudflat and relevant at the higher mudflat.

The two locations respond differently to wind from the SW and NE. At the lower mudflat, SSC is highest during NE wind (largest circles in the NE quadrant of Figure 11c,d), despite higher waves occurring during western winds (blue colors in the NW and SW quadrant of Figure 11d). The current-induced bed shear stress is comparable for NW and NE winds (Figure 11c). This suggests that the high sediment concentration during NE winds results from advection, rather than local resuspension. In contrast, both SSC and wave induced bed shear stress are highest during NW winds at the higher mudflat (Figure 11f), implying a large relative contribution of local reususpension.

Eventually, the increase in sediment concentration with NE wind (especially for the lower mudflat) suggests the presence of a sediment source east of the observation locations. This may result from transport over the tidal divides, as suggested by Sassi et al. [29] and Duran-Matute et al. [30]. Alternatively (or additionally), tidal divides can become temporal sediment sinks [44] from which sediment is resuspended during larger winds following a calm period.

4.5. Conceptual Model of Wind-Induced Sediment Transport and Storage in Intertidal Areas

The strong dependency of sediment transport on wind speed and direction is related to the hydrodynamics (Section 4.3), but also to sediment concentration (Section 4.4). This is illustrated in Figure 12.

During dominant wind conditions the residual sediment transport is directed from the tidal channel to the higher flats: the transport is controlled by the channel, and the sediment concentration is relatively low (phase 1). The sediment deposits onto the more elevated intertidal zones, including where present, the tidal divides (phase 2). However, the majority of that sediment is only temporally deposited. Even moderate winds having directions opposite to the dominant winds generate large down-channel residual transport (phase 3). In this case the sediment fluxes are characterized by very large sediment concentrations. The observation that sediment is easily eroded from this temporal sediment storage implies that the material is poorly consolidated (even after weeks of phase 1 and phase 2 conditions). This conclusion is important for our understanding of the long-term morphodynamics of muddy intertidal flat systems.

Our results are particularly important for muddy areas where the dominant wind direction is, within a certain directional spreading, aligned with the coastline, and the tidal currents are also primarily aligned with the coastline. The role of wind-driven currents is much less pronounced when the dominant wind direction is primarily normal to the coastline, or when the tidal currents are primarily in the cross-shore direction. The angle between wind and coastline depends strongly on the larger-scale geological setting, such as river mouths in estuaries or the large-scale coastal development. The alignment of along-shore tidal currents with respect to the coastline is more strongly influenced by local conditions. Many tidal flats, especially along exposed coastlines with low wave energy, develop extensive, mildly sloping foreshores where cross-shore tidal currents are stronger than long-shore currents. Long-shore tidal currents are more common in estuarine environments where tidal channels encroaching the estuarine embankments lead to steeper cross-shore profiles, or in lagoons where sheltering barriers limit the number of cross-shore tidal channels, leading to the development of long-shore tidal channels.

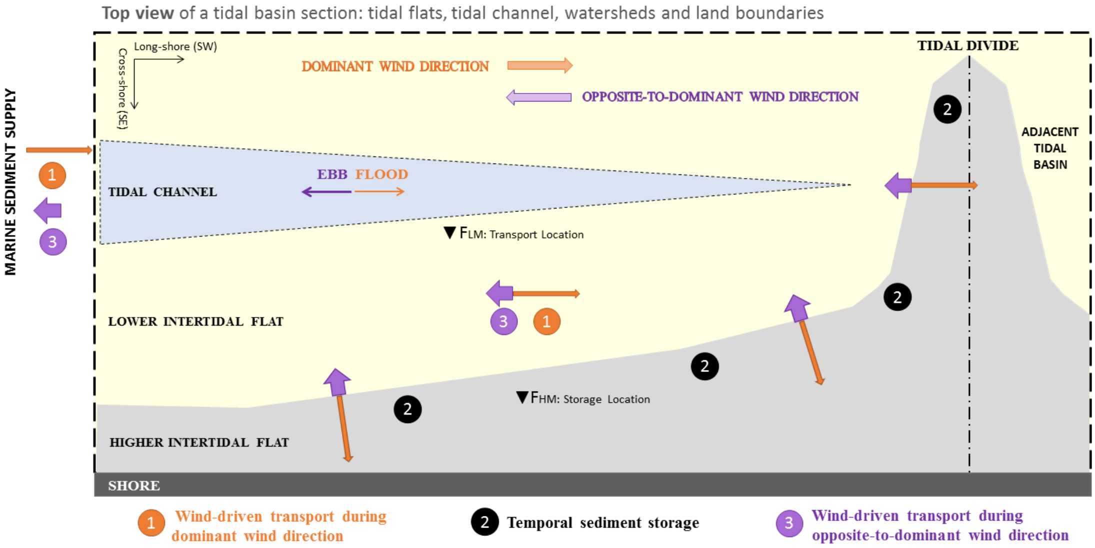

Figure 12. Conceptual model of wind-induced sediment transport and storage within our study site. Phase 1 (orange arrows): wind driven transport during dominant wind direction (corresponding to the direction of flood currents). Phase 2: temporal storage following phase 1. Phase 3 (purple arrows, in ebb direction): transport opposite to the dominant wind direction. The widths of the arrows relate to the SSC in the net fluxes (larger for the opposite-to-dominant wind case), whereas the lengths of the arrows relate to the number of occurrences in time (larger for the dominant wind case). The two investigated locations are included in the scheme. The transport location F_{LM} is current dominated (i.e., advection controls the SSC), has large gross fluxes but small net fluxes, and it is characterized by limited bed level changes. At the storage location F_{HM}, where both advection and resuspension contribute to the SSC, the net fluxes are controlled by wind speed and direction and it is characterized by larger and continuous changes in bed level.

5. Conclusions

Waves, water levels, flow, and sediment concentrations were measured on an intertidal flat in a meso-tidal system. Based on these data, the interactions among wind-waves, tide-induced flow, and wind-driven flow were investigated and the effects of this interaction on the sediment transport were explored.

The flow velocity resulting from the non-linear interaction between tide and wind-driven flow was estimated by applying the momentum balance equation and using field data to quantify its terms. The tide-induced pressure gradient, the wind-induced stress, and the bed shear stress dominate the balance, and can be used to model the flow velocity induced by tide and wind. The model shows that the magnitude of wind-driven flow decreases (increases) for increasing (decreasing) tidal flow amplitude. At sites characterized by a relatively weak tide-induced flow ($\sim$0.2 m/s) the wind is able to reverse the direction of the tidal flow also at moderate wind speeds ($\sim$10 m/s). Therefore, wind-induced reversal of the tidal flow is a common phenomenon in environments characterized by small tidal flow amplitudes. The model predictions of the net flow, and of the wind speed at which the tidal flow reverses, show good agreement with data.

The intratidal SSC asymmetry is highly influenced by wind speed, but also by wind direction, as the latter affects the fetch length and therefore the areas prone to resuspension. Highest sediment concentrations were not observed during the highest wave-induced stress, but during one wind event that followed a period of low/moderate wind from a direction opposite to the dominant wind direction.

This study therefore shows that the crucial role of wind in tidal flat sediment dynamics not only relates to the wave-induced resuspension, but also to the generation of wind-driven flows enhancing the tide-induced advection of sediment, ultimately affecting the net sediment transport and hence the morphodynamics of intertidal areas.

Our results further suggest that sediments can be temporarily stored in the shallower areas of the intertidal system, and then easily resuspended and advected during wind events. These storage environments accumulate sediments in conditions of low/moderate wind having the same direction as the tide-induced residual transport, and release sediment during events with winds having opposite directions. Fairly short windy periods opposite to tide-induced residual transport may in this way balance the residual transport of sediment that occurred over longer time periods in calm wind conditions. This temporal storage of sediment in combination with wind-driven transport is crucial for understanding short- and long-term sediment dynamics in muddy systems, but is in general poorly accounted for in literature. We expect that the results provided by this study are especially relevant at locations where the dominant wind direction and the main tidal flow direction are aligned with the coastline (such as in estuaries and lagoons, but less so for exposed, broad muddy coastlines).

Author Contributions: Data curation, I.C., P.L.M.d.V.; Project administration: B.C.v.P.; Supervision, D.S.v.M. and B.C.v.P.; Writing original draft: I.C. and B.C.v.P.; Formal analysis, writing review and editing, I.C., P.L.M.d.V., D.S.v.M., A.J.H.M.R., J.C.W. and B.C.v.P. All authors have read and agreed to the published version of the manuscript.

Funding: This study is part of the research program "Sediment for Salt Marshes: Physical and Ecological Aspects of a Mud Motor" with project number 13888, which is partly financed by The Netherlands Organization for Scientific Research (NWO).

Acknowledgments: The authors acknowledge the Netherlands Organization for Scientific Research (NWO) for the project financing. The authors thank two anonymous reviewers for their constructive comments and suggestions.

Conflicts of Interest: The authors declare no conflict of interest.

Appendix A. Bed Shear Stress Induced by Wave–Current Interaction

The bed shear stress resulting from the combined action of waves and currents is estimated using the wave-current-interaction (WCI) models proposed by Soulsby [41]. The mean bed shear stress resulting from the interaction of currents and waves is estimated as:

$$\tau_m = \tau_c \left[1 + 1.2 \left(\frac{\tau_w}{\tau_c + \tau_w} \right)^{3.2} \right] \tag{A1}$$

with τ_c current-induced shear stress, and τ_w wave-induced shear stress. The usage of the mean bed shear stress as expressed in Equation (A1) is suitable when estimating the effect of waves on the current-induced flow, e.g., [16].

The current-induced shear stress is estimated as:

$$\tau_c = \rho_w c_{f_c} u^2 \tag{A2}$$

with c_{f_c} the current-related friction coefficient and $u = (u_x, u_y)$ the flow velocity magnitude. The bed friction coefficient depends on the roughness height z_0:

$$\frac{1}{\sqrt{c_{f_c}}} = \frac{1}{\kappa} \left(\ln \left(\frac{h}{z_0} \right) - 1 \right) \tag{A3}$$

The estimation of the roughness height z_0 is not straightforward, as it depends on the skin friction (sediment diameter), on the presence of bed forms (e.g., current and wave induced ripples), on the hydrodynamics, and among other factors, on sediment stratification, e.g., [16,45,46]. Values of the current related friction coefficient c_{f_c} available in literature suggest a variability of the parameter in the range 0.001–0.004, e.g., [16,41,45–50]. A value of 0.002 has been selected, based on which the roughness length z_0 has been estimated along the full measurement period, as a function of water depth (Equation (A3)). The so-estimated z_0 values are one order of magnitude higher than the values obtained from a definition based on the grain size only (e.g., $z_0 = \frac{k_s}{30} = D_{50}/12$).

The wave-induced shear stress is estimated based on the wave-friction factor f_w and the wave orbital velocity at the bottom U_δ:

$$\tau_w = \frac{1}{2}\rho_w f_w {U_\delta}^2 \tag{A4}$$

The wave orbital velocity is estimated using the linear wave theory:

$$U_\delta = \frac{\pi H}{T} \cdot \frac{1}{\sinh(kh)} \tag{A5}$$

The wave number k is obtained by resolving the dispersion relationship using a polynomial approximation, based on the measured water depth and mean wave period following [51]. The wave friction factor f_w is estimated using the formulation proposed by Soulsby et al. [45] :

$$f_w = min\left[0.3, 1.39\left(\frac{U_\delta T}{2\pi z_0}\right)\right] \tag{A6}$$

where z_0 is the bed roughness.

References

1. Piersma, T.; de Goeij, P.; Tulp, I. An evaluation of intertidal feeding habitats from a shorebird perspective: Towards relevant comparisons between temperate and tropical mudflats. *Neth. J. Sea Res.* **1993**, *31*, 503–512. [CrossRef]
2. Ysebaert, T.; Meininger, P.L.; Meire, P.; Devos, K.; Berrevoets, C.M.; Strucker, R.C.; Kuijken, E. Waterbird communities along the estuarine salinity gradient of the Schelde estuary, NW-Europe. *Biodivers. Conserv.* **2000**, *9*, 1275–1296. [CrossRef]
3. Barbier, E.B.; Hacker, S.D.; Kennedy, C.; Kock, E.W.; Stier, A.C.; Sillman, B.R. The value of estuarine and coastal ecosystem services. *Ecol. Monogr.* **2011**, *81*, 169–193. [CrossRef]
4. Kirwan, M.L.; Megonigal, J.P. Tidal wetland stability in the face of human impacts and sea-level rise. *Nature* **2013**, *504*, 53–60. [CrossRef]
5. Cloern, J.E.; Knowles, N.; Brown, L.R.; Cayan, D.; Dettinger, M.D.; Morgan, T.L.; Schoellhamer, D.H.; Stacey, M.T.; van der Wegen, M.; Wagner, R.W.; et al. Projected evolution of California's San Francisco bay-delta-river system in a century of climate change. *PLoS ONE* **2011**. [CrossRef]
6. Van Goor, M.A.; Zitman, T.J.; Wang, Z.B.; Stive, M.J. Impact of sea-level rise on the morphological equilibrium state of tidal inlets. *Mar. Geol.* **2003**, *202*, 211–227. [CrossRef]
7. Maan, D.C.; van Prooijen, B.C.; Wang, Z.B. Progradation Speed of Tide-Dominated Tidal Flats Decreases Stronger Than Linearly with Decreasing Sediment Availability and Linearly with Sea Level Rise. *Geophys. Res. Lett.* **2019**. [CrossRef]
8. Temmerman, S.; Meire, P.; Bouma, T.J.; Herman, P.M.J.; Ysebaert, T.; De Vriend, H.J. Ecosystem-based coastal defence in the face of global change. *Nature* **2013**, *504*, 79–83. [CrossRef]
9. Baptist, M.J.; Gerkema, T.; van Prooijen, B.; van Maren, D.; van Regteren, M.; Schulz, K.; Colosimo, I.; Vroom, J.; van Kessel, T.; Grasmeijer, B.; et al. Beneficial use of dredged sediment to enhance salt marsh development by applying a 'Mud Motor'. *Ecol. Eng.* **2019**, *127*, 312–323. [CrossRef]
10. Kirby, R. Minimising harbour siltation—Findings of PIANC Working Group 43. *Ocean Dyn.* **2011**, *61*, 233–244. [CrossRef]
11. Pontee, N.I. Saltmarsh loss and maintenance dredging in estuaries. *Proc. Inst. Civ. Eng. Mar. Eng.* **2004**. [CrossRef]
12. De Vet, P.L.M.; Prooijen, B.C.; Colosimo, I.; Ysebaert, T.; Herman, P.M.J.; Wang, Z.B. Sediment Disposals in Estuarine Channels Alter the Eco-Morphology of Intertidal Flats. *J. Geophys. Res. Earth Surf.* **2020**, *125*. [CrossRef]

13. Wang, Z.B.; Hoekstra, P.; Burchard, H.; Ridderinkhof, H.; Swart, H.E.D.; Stive, M.J.F. Ocean & Coastal Management Morphodynamics of the Wadden Sea and its barrier island system. *Ocean Coast. Manag.* **2012**, *68*, 39–57. [CrossRef]
14. Daidu, F.; Yuan, W.; Min, L. Classifications, sedimentary features and facies associations of tidal flats. *J. Palaeogeogr.* **2013**, *2*, 66–80. [CrossRef]
15. Van Straaten, L.M.J.U. Sedimentation in Tidal Flat Areas. *Bull. Can. Pet. Geol.* **1961**, *9*, 203–226.
16. Faria, A.F.G.; Thornton, E.B.; Stanton, T.P.; Soares, C.V.; Lippmann, T.C. Vertical profiles of longshore currents and related bed shear stress and bottom roughness. *J. Geophys. Res. Ocean.* **1998**, *103*, 3217–3232. [CrossRef]
17. Soulsby, R.; Clarke, S. Bed Shear-stresses Under Combined Waves and Currents on Smooth and Rough Beds. *Hydraul. Res. Rep.* **2005**, *1905*, TR 137.
18. Bassoullet, P.; Le Hir, P.; Gouleau, D.; Robert, S. Sediment transport over an intertidal mudflat: Field investigations and estimation of fluxes within the 'Baie de Marennes-Oleron' (France). *Cont. Shelf Res.* **2000**, *20*, 1635–1653. [CrossRef]
19. Carniello, L.; D'Alpaos, A.; Defina, A. Modeling wind waves and tidal flows in shallow micro-tidal basins. *Estuarine Coast. Shelf Sci.* **2011**, *92*, 263–276. [CrossRef]
20. Friedrichs, C.T. *Tidal Flat Morphodynamics: A Synthesis*; Elsevier Inc.: Amsterdam, The Netherlands, 2012; Volume 3, pp. 137–170. [CrossRef]
21. Green, M.O.; Coco, G. Review of wave driven sediment resuspension and transport in estuaries. *Rev. Geophys.* **2014**, *52*, 77–117. [CrossRef]
22. Hir, P.L.; Roberts, W.; Cazaillet, O.; Christie, M.; Bassoullet, P.; Bacher, C. Characterization of intertidal # at hydrodynamics. *Cont. Shelf Res.* **2000**, *20*, 1433–1459.
23. Mariotti, G.; Fagherazzi, S. Wind waves on a mudflat: The influence of fetch and depth on bed shear stresses. *Cont. Shelf Res.* **2013**, *60*, S99–S110. [CrossRef]
24. Zhu, Q.; van Prooijen, B.C.; Wang, Z.B.; Yang, S.L. Bed-level changes on intertidal wetland in response to waves and tides: A case study from the Yangtze River Delta. *Mar. Geol.* **2017**, *385*, 160–172. [CrossRef]
25. Baeye, M.; Fettweis, M.; Voulgaris, G.; Van Lancker, V. Sediment mobility in response to tidal and wind-driven flows along the Belgian inner shelf, southern North Sea. *Ocean Dyn.* **2011**, *61*, 611–622. [CrossRef]
26. Christiansen, C.; Vølund, G.; Lund-Hansen, L.C.; Bartholdy, J. Wind influence on tidal flat sediment dynamics: Field investigations in the Ho Bugt, Danish Wadden Sea. *Mar. Geol.* **2006**, *235*, 75–86. [CrossRef]
27. Mariotti, G.; Fagherazzi, S. Asymmetric fluxes of water and sediments in a mesotidal mudflat channel. *Cont. Shelf Res.* **2011**, *31*, 23–36. [CrossRef]
28. Talke, S.A.; Stacey, M.T. Suspended sediment fluxes at an intertidal flat: The shifting influence of wave, wind, tidal, and freshwater forcing. *Cont. Shelf Res.* **2008**, *28*, 710–725. [CrossRef]
29. Sassi, M.; Duran-Matute, M.; van Kessel, T.; Gerkema, T. Variability of residual fluxes of suspended sediment in a multiple tidal-inlet system: The Dutch Wadden Sea. *Ocean Dyn.* **2015**, *65*, 1321–1333. [CrossRef]
30. Duran-Matute, M.; Gerkema, T.; De Boer, G.J.; Nauw, J.J.; Gräwe, U. Residual circulation and freshwater transport in the Dutch Wadden Sea: A numerical modelling study. *Ocean Sci.* **2014**, *10*, 611–632. [CrossRef]
31. Postma, H. Transport and accumulation of suspended matter in the Dutch Wadden Sea. *Neth. J. Sea Res.* **1961**, *1*, 148–190. [CrossRef]
32. Bartholomä, A.; Flemming, B.W. Progressive grain-size sorting along an intertidal energy gradient. *Sediment. Geol.* **2007**, *202*, 464–472. [CrossRef]
33. Schulz, K.; Gerkema, T. Corrigendum to 'An inversion of the estuarine circulation by sluice water discharge and its impact on suspended sediment transport.' [Estuarine, Coastal and Shelf Science 200 (2018) 31-40] (S0272771417306194) doi.org/10.1016/j.ecss.2017.09.031. *Estuarine Coast. Shelf Sci.* **2018**, *207*, 510. [CrossRef]
34. Goring, D.G.; Nikora, V.I. Despiking Acoustic Doppler Velocimeter Data. *J. Hydraul. Eng.* **2002**, *128*, 117–126. [CrossRef]
35. Codiga, D.L. *Unified Tidal Analysis and Prediction Using the UTide Matlab Functions*; Technical Report 2011-01; Graduate School of Oceanography, University of Rhode Island: Narragansett, RI, USA, 2011. [CrossRef]
36. Tucker, M.; Pitt, E. *Waves in Ocean Engineering*; Elsevier: Amsterdam, The Netherlands, 2001; p. 521.
37. Andersen, T.; Pejrup, M. Suspended sediment transport on a temperate, microtidal mudflat, the Danish Wadden Sea. *Mar. Geol.* **2001**, *173*, 69–85. [CrossRef]
38. Lin, W.; Sanford, L.P.; Suttles, S.E.; Valigura, R. Drag Coefficients with Fetch-Limited Wind Waves. *J. Phys. Oceanogr.* **2002**. [CrossRef]

39. Wu, J. Wind-stress coefficients over sea surface near neutral conditions—A revisit. *J. Phys. Oceanogr.* **1980**. [CrossRef]
40. Wu, J. Wind-stress coefficients over sea surface from breeze to hurricane. *J. Geophys. Res.* **1982**. [CrossRef]
41. Soulsby, R. Bed shear-stresses due to combined waves and currents. In *Advances in Coastal Morphodynamics: An Overview of the G-8 Coastal Morphodynamics Project*; Delft Hydraulics: Delft, The Netherlands, 1995; pp. 20–23.
42. De Vet, P.L.M.; van Prooijen, B.C.; Schrijvershof, R.A.; van der Werf, J.J.; Ysebaert, T.; Schrijver, M.C.; Wang, Z.B. The Importance of Combined Tidal and Meteorological Forces for the Flow and Sediment Transport on Intertidal Shoals. *J. Geophys. Res. Earth Surf.* **2018**, *123*, 2464–2480. [CrossRef]
43. Speerstra, H.J. *Estimating the Roughness of Muddy Beds*; Technical Report; Delft University of Technology: Delft, The Netherlands, 2018.
44. Bartholdy, J.; Christiansen, C.; Kunzendorf, H. Long term variations in backbarrier salt marsh deposition on the Skallingen peninsula—The Danish Wadden Sea. *Mar. Geol.* **2004**, *203*, 1–21. [CrossRef]
45. Soulsby, R.L.; Hamm, L.; Klopman, G.; Myrhaug, D.; Simons, R.R.; Thomas, G.P. Wave-current interaction within and outside the bottom boundary layer. *Coast. Eng.* **1993**, *21*, 41–69. [CrossRef]
46. Fan, R.; Zhao, L.; Lu, Y.; Nie, H.; Wei, H. Impacts of Currents and Waves on Bottom Drag Coefficient in the East China Shelf Seas. *J. Geophys. Res. Ocean.* **2019**, *124*, 7344–7354. [CrossRef]
47. ASCE. Friction factors in open channels. *J. Hydraul. Div. ASCE* **1963**, *89*, 97–143.
48. Sternberg, R.W. Friction factors in tidal channels with differing bed roughness. *Mar. Geol.* **1968**. [CrossRef]
49. Verney, R.; Brun-Cottan, J.C.; Lafite, R.; Deloffre, J.; Taylor, J.A. Tidally-induced shear stress variability above intertidal mudflats in the macrotidal seine estuary. *Estuaries Coasts* **2006**, *29*, 653–664. [CrossRef]
50. Pascolo, S.; Petti, M.; Bosa, S. On the Wave Bottom Shear Stress in Shallow Depths: The Role of Wave Period and Bed Roughness. *Water* **2018**, *10*, 1348. [CrossRef]
51. Hunt, S.; Bryan, K.R.; Mullarney, J.C. The influence of wind and waves on the existence of stable intertidal morphology in meso-tidal estuaries. *Geomorphology* **2015**, *228*, 158–174. [CrossRef]